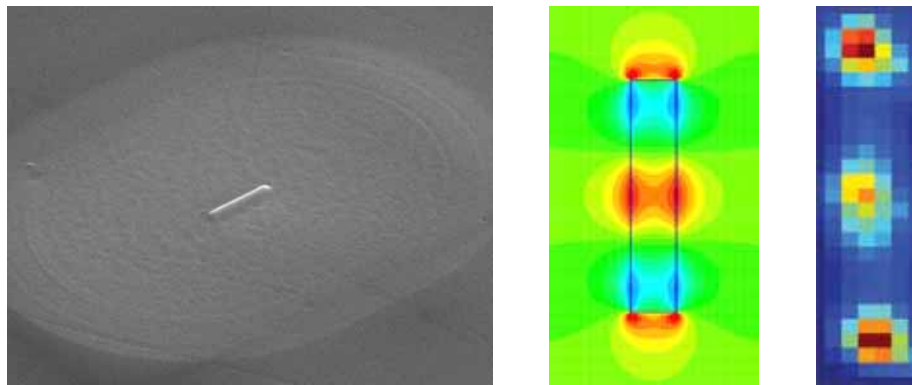


Cathodoluminescence of plasmonic nanowire modes

Ernst Jan Vesseur

Supervised by drs. René de Waele and prof. dr. Albert Polman

In collaboration with Henri J. Lezec, Luke A. Sweatlock, Carrie E. Ross, Woo Lee,
Ulrich Gösele and Harry A. Atwater



Research project for the masters degree in
Experimental Physics at Utrecht University, The Netherlands
May 2006 - January 2007

The Center for Nanophotonics
FOM-Institute AMOLF
Amsterdam, The Netherlands

California Institute of Technology
Pasadena, CA, USA



Abstract

Surface plasmon polaritons (SPPs) provide a route towards miniaturization of optical components, which has many possible applications in the field of information technology.

The most basic component in guiding of signals is a wire. A gold wire is able to support SPPs, and has interesting optical properties that are not available to conventional waveguides. In this work, we study the photonic properties of gold nanowires, or nanorods, with diameter on the order of 100nm and lengths of 350nm to several microns, using cathodoluminescence (CL) spectroscopy.

Nanorods or rod-like structures were fabricated using e-beam lithography, template growth and Focused Ion Beam (FIB) milling.

FIB is presented as a tool for nanophotonic sample preparation and it is shown how the high resolution of the ion beam in combination with the homogeneity of a single crystal gold sample allows for fabrication of plasmonic nanostructures with unprecedented detail.

Finite-difference time-domain (FDTD) simulations have been performed on nanorod geometries to study plasmonic modes that are supported by this configuration. It is shown that gold nanorods have organ pipe-like resonances with an integer number of electric field antinodes on the rod. Next to isolated rods, also elongated gold ridges on a single crystal gold surface are shown to have geometrical resonances. The simulations also show that the wire mode resonances have shorter wavelength than their plain film SPP counterparts.

We made use of the small beam spot of a modern Scanning Electron Microscope (SEM) to very locally ($< 10\text{nm}$) excite resonances on gold nanorods. By analyzing the CL signal as a result of this excitation we find both the excitation efficiency at a location as well as the spectrum of modes corresponding to the sample. These measurements show that the efficiency of wire mode excitation by the electron beam is modulated along the wire, which is in agreement with the electric field in simulation.

Contents

1	Introduction	5
2	Focused Ion Beam as a tool for nanophotonic sample preparation	7
2.1	Introduction	7
2.1.1	Applications of FIB	9
2.2	Methods and Results	10
2.2.1	FIB system	10
2.2.2	Single crystal gold	10
2.2.3	Patterning of gold nanorods	12
2.2.4	Patterning of an evaporated gold film on quartz	15
2.2.5	Sample analysis	16
3	FDTD simulations of gold nanorods	19
3.1	Methods	19
3.2	Results	20
3.2.1	500nm nanorod	20
3.2.2	Transverse resonances	23
3.2.3	Subtract-rod	25
3.3	Conclusions	26
4	Cathodoluminescence measurements on plasmonic nanostructures	27
4.1	Introduction	27
4.2	Setup	27
4.3	CL measurements on gold nanorods	28
4.3.1	E-beam and lift-off nanorods	28
4.3.2	Subtracted rods	35
4.3.3	Template grown nanorods	36
4.4	Annular nanoresonators in gold	39
4.4.1	Single rings	39
4.4.2	Annular nanoresonators	40
4.5	Conclusions	40

Chapter 1

Introduction

Surface plasmon polaritons (SPPs) are collective oscillations of free electrons at the surface of a metal [1]. SPPs offer a way to manipulate light on a sub-wavelength scale. The strong localization of the electric field in plasmonic structures holds promises for the construction of nanophotonic devices [2, 3, 4].

A possibly important part of such devices is a metal nanowire [5]. Nanowires have been shown to support plasmon propagation [6, 7]. Shorter nanowires (nanorods) can sustain standing plasmon waves because the wire ends reflect the oscillation. This has been studied in bulk [8, 9] and using near-field techniques [10, 11]. It was shown that the wire modes behave like organ pipe modes, and that in the optical regime the dispersive material properties become important [12].

Nanowires can thus be used for plasmon transport, but even the nanowire by itself can be used as a plasmonic application because of the high field enhancement near wire ends and between wires [13, 14].

This thesis describes how we used cathodoluminescence as a new method to probe nanowire mode behaviour.

Cathodoluminescence (CL) is the luminescence of a material as a result of excitation by electron impact. CL has been used to generate light and plasmons [15, 16]. Furthermore, it was shown that using a very small beam width plasmon propagation could be measured [17, 18] and that CL can be used to map the spatial properties of resonances [19] on a nanoscale.

We discuss the use of CL in a Scanning Electron Microscope (SEM). The SEM is designed to have a very small electron beam width, which makes it a perfect setup to exploit the high sensitivity of luminescence on the nanoscale electron beam position. Combined with conventional high resolution spectroscopy this system allows for a detailed characterization of nanostructures.

Nanowires as plasmon resonators are an interesting model to verify the spatially varying excitation of modes and the dependence of excitation efficiency on modal field [20]. It has also been suggested that CL emission is related to the local density of states (LDOS) at the electron impact location. In the case of nanowires, the LDOS pattern is modulated along the wire [21].

Sample fabrication was partly done using Focused Ion Beam (FIB). We used FIB for the fabri-

cation of nanowire-like structures. The FIB work is described in detail in chapter 2, where FIB is more generally presented as a tool for nanofabrication.

In order to compare CL measurements performed on nanowire geometries to the electric field of modes in such structures, we simulated these modes using a Finite-Difference Time-Domain (FDTD) technique. This work is described in chapter 3. We find resonances and mode profiles that agree with the organ pipe-like behaviour we expected.

Chapter 4 contains the CL measurements. Three different types of nanowires are investigated. It is shown that the CL signal from a nanowire has a number of maxima on the wire that depend on the detection wavelength. This is a strong indication that we are indeed probing mode profiles. Finally measurements on annular structures are presented that also indicate that these structures have a strong mode behavior.

Chapter 2

Focused Ion Beam as a tool for nanophotonic sample preparation

This chapter gives a short introduction into Focused Ion Beam (FIB), and continues with an overview of the results we obtained by patterning sample substrates with nanostructures using FIB.

2.1 Introduction

In the early 1950's Scanning Electron Microscopy (SEM) was a well developed technique for studying features on a substrate with a spatial resolution of ~ 50 nm [22] (today: $1 - 20$ nm). It has taken until 1975 with the discovery of a Liquid Metal Ion Source (LMIS) before an ion beam of reasonable beam current could be focused to a sub-micron beam spot.

Before the discovery of the LMIS it had not been possible to generate either sufficient ion beam current or a sufficiently narrow beam. Figure 2.1 shows a typical gallium LMIS. The tungsten coil forms a reservoir for liquid gallium, that is liquified through a current in the tungsten wires. The gallium wets the protruding part of the source, that is shaped such that the radius of curvature of the tip is of the order of 100 nm. By application of a moderate (kV) voltage between the tip and an extractor (figure 2.1), the electric field in the direct vicinity of this tip becomes high enough to ionize the metal ions. The result is a sub-nanometer virtual ion source.

Although ion beams of many different metal ions have successfully been created [23], gallium is the only metal that was ultimately used in commercial systems, because of its superior wetting properties.

In every FIB system the ion beam is accelerated, directed and focused by a lens system that is very similar to that in an electron beam column (figure 2.1).

When an ion beam hits a sample surface, a great number of processes occur. Figure 2.2 illustrates the phenomena that are of main importance for applications.

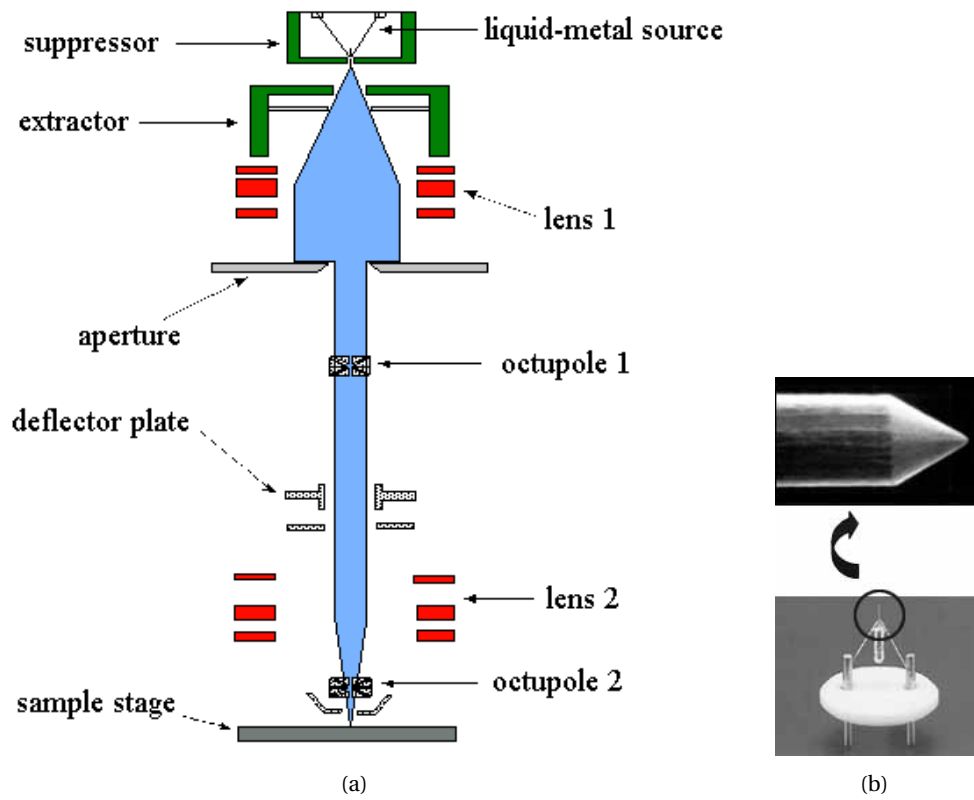


Figure 2.1: (a) Schematic of a FIB column. After ion extraction the beam is collimated and focused by multiple lenses. (b) Typical Liquid Metal Ion Source. This specimen is a gallium source.

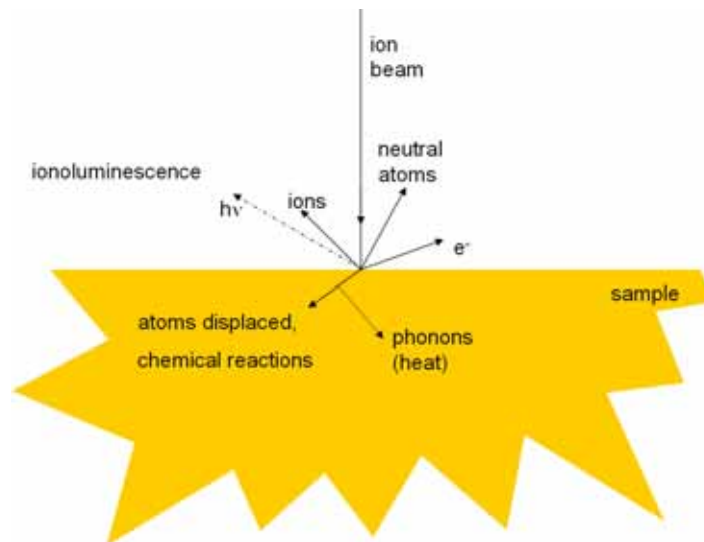


Figure 2.2: Ion hitting a surface: sputtering, secondary electrons, ion implantation, displacement, ionoluminescence.

2.1.1 Applications of FIB

Imaging

Similar to an electron beam, the ion beam can be deflected in the column, which allows for focusing at any desired position on the sample within the 'field of view'. The secondary electrons that are generated during ion exposure can be detected by ordinary electron detectors. Therefore every modern FIB system can be used as a scanning ion microscope, by setting it to an image mode where ion beam scanning and electron detection are synchronized. In a dual beam system (i.e. with an electron column and an ion column), one detector detects secondary electrons that result from interaction of the sample with either the ion beam or the electron beam. In case the detector bias is set to a negative value, backscattered ions can be detected.

In imaging mode, the FIB reveals sample geometry in roughly the same way the electron beam does.

There are some differences in the interaction of the ion beam and electron beam with the sample, however. Apart from the destructive character of the ion beam, the secondary electron contrast generated either by e-beam or ion beam is different. The secondary electron generation by the ion beam is very sensitive to the crystal lattice orientation of the sample, which is less so with the electron beam. This is caused by channeling of ions through the crystal, which is strongly dependent on the angle of incidence. This makes FIB very suitable for imaging grains [24] of different lattice orientations.

Imaging mode is furthermore used to focus the ion beam for applications described in the next paragraph.

FIB milling and deposition

A FIB with sufficient beam current sputters away material. Since modern beams have a high spatial resolution, i.e. a nanometer beam spot, milling can be done at a very small scale (~30 nm). Milling of samples to form nanostructures is currently the most important application for FIB. Apart from fabrication, milling can also be used to investigate the inner structure of a sample.

Milling can be performed in the presence of a vapour. This allows for higher milling rates or selective etching of different material composites.

Other gases enable the FIB to deposit material on the sample surface. Mostly platinum- and carbon containing compounds are used.

Similar to effects in ion imaging, also the etch rate is influenced by crystal lattice orientation. This can be very important in polycrystalline materials. Here the different milling rates can increase additional roughness by etching some grains faster than other grains.

Milling rates can also vary considerably between different types of materials. Therefore, the first step in a new nanofabrication process is perform dose tests to check etching rates. Beam current, dwell times and pixel step values have to be optimized in order to reach both sufficient pattern definition accuracy and milling speed. A smaller beam current for instance gives a lower

milling rate, but increases accuracy. When minimization of total milling time is important the choice of beam current is a tradeoff.

After ion irradiation with the parameters of choice, the depth can be measured from a scanning electron micrograph, taking into account the angle between the sample normal and the electron beam. This method is quick and perfectly suitable for objects with sharp edges and a moderate aspect ratio, but is less precise in other cases. In those cases it is an option to calibrate the mill depth with AFM or STM.

The link between dwell time and mill depth is only linear for very shallow structures (~ 10 nm). For a long dwell time, there is an effect that disturbs this linear dependence. Next to the beam spot, there will be a wall of material that has not yet been removed. Effectively, when milling at this point, the ion beam will be incident under an angle. This increases the milling rate. The result is that scanning in a certain direction increases the etch depth while performing the scan, because the increased etch rate on the edge will make the pattern deeper and deeper. This problem can be solved by scanning with multiple passes, where each pass has limited pixel dwell times. A second effect that influences milling rate, is backsputtering. In a deep, high-aspect ratio pattern, more atoms will be backspattered onto the walls at the edge of the pattern than in a shallow pattern.

2.2 Methods and Results

2.2.1 FIB system

A FEI Nova 600 system (figure 2.3) was used for patterning. This is a dual beam system; maximum acceleration voltage of the e^- and Ga^+ column both is 30 kV.

The system comes with software that allows for use of bitmaps. This enables per-pixel control of dwell times for a rectangular pattern. On this particular setup, it is not possible to choose the order in which the pixels are being scanned.

In case the pixel distance as set by the user becomes comparable to the smallest step of the digital analog converter (DAC) of the beam deflector, an effect, known as aliasing (i.e. some pixels are double exposed and others are skipped), can become an issue. In fact, this is only a problem at low magnification, where the DAC step becomes larger than the milling resolution.

The horizontal and vertical lines in figure 2.4 are a result of aliasing. The design structure was a homogeneous rectangle.

2.2.2 Single crystal gold

Coin-shaped single crystal gold substrates, grown using the Czochralski process [25] and polished on the $\langle 111 \rangle$ surface, were obtained from Surface Preparation Laboratory, Zaandam, the Netherlands. With SEM a lateral roughness was found of < 10 nm.

Since the ion beam milling rate strongly depends on crystal orientation, the single-crystallinity of this sample was expected to be a great advantage in acquiring a high degree of depth control.



Figure 2.3: A Nova 600 FIB workstation.

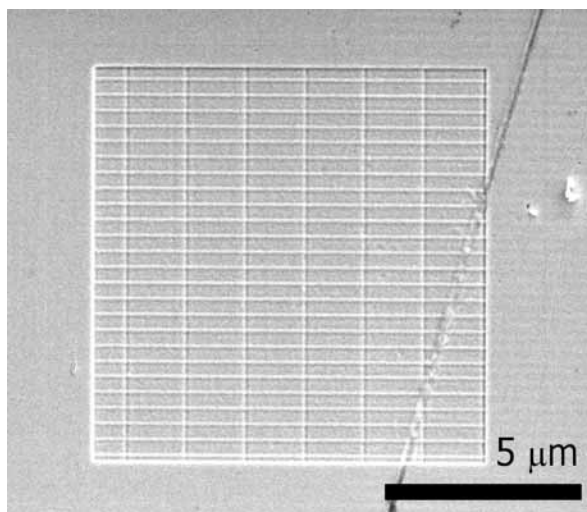


Figure 2.4: An example of aliasing problems. This is the result of etching a square with the ion beam set to a low magnification ($2490\times$). In this case one DAC step corresponds to 13 nm on the sample.

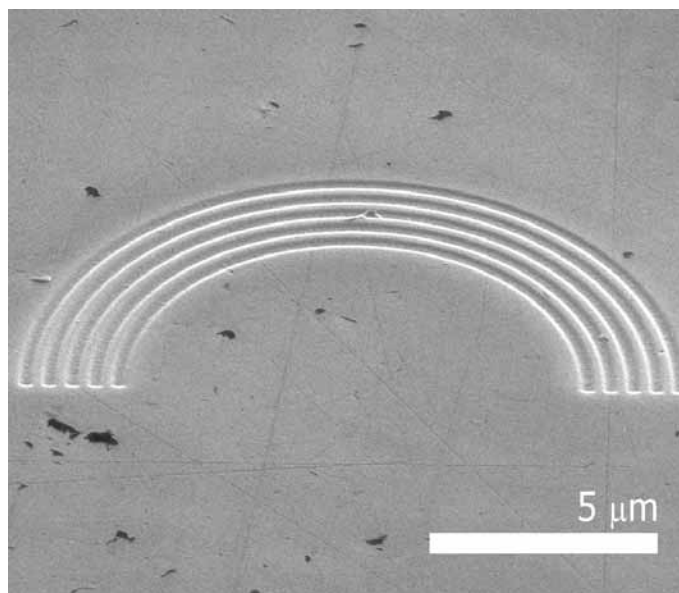


Figure 2.5: Scanning electron micrograph of a half-circle groove pattern made with FIB on single crystal gold. A 1500 pixel wide bitmap file was used to define the structure. It was scanned in 39 passes using a 1 μ s dwell time per pixel and a 87 pA beam current.

A beam current of 87 pA gave a high milling rate with acceptable resolution on the single crystal gold. A pixel step of 14 nm was sufficiently small to retain smoothness of the sample during etching of the surface.

Figures 2.5, 2.6, 2.7 and 2.8 give examples of geometries that were fabricated on the slab of single crystal gold.

2.2.3 Patterning of gold nanorods

Aside from the patterning of substrates FIB can also be used to pattern existing structures. Figure 2.9 depicts a schematic of a gold nanorod patterned with a grating at both ends of the rod. We want to mill such a structure to investigate the influence of a grating on confinement of surface plasmon modes on a wire.

Metal nanorods were obtained by electrodeposition in alumina templates [26], of which the synthesis was performed by Woo Lee¹. After dissolution of the alumina template, the rods were transferred to a solution of anhydrous ethanol.

Both 60 nm diameter and 200 nm diameter rods were synthesized using this method. Dispersion in length of each of the types gave a range of 1 μ m to \sim 20 μ m in length. After deposition on a silicon substrate most of the rods formed clusters although some rods were found isolated on the substrate. Besides, longer rods could be isolated more easily, but they also tended to bend.

¹Gösele group, Max Planck Institute of Microstructure Physics, Halle, Germany

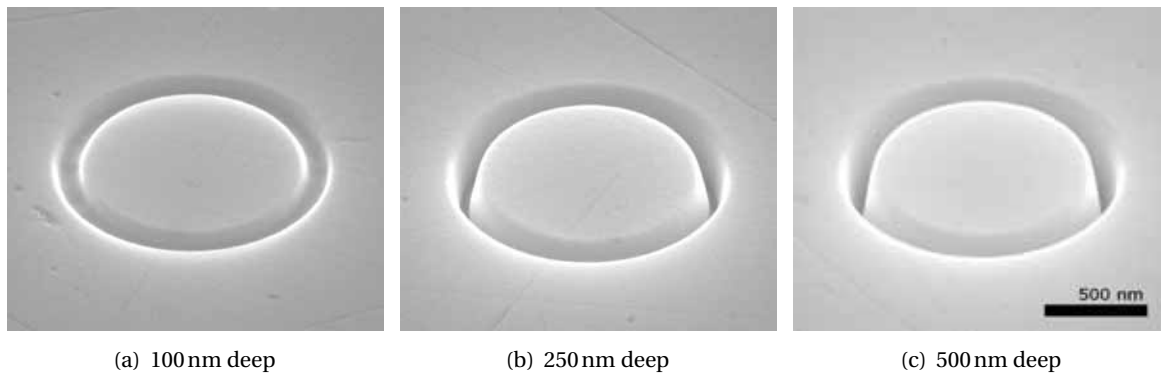


Figure 2.6: SEM image of rings with different depths, milled in the single crystal gold surface. The images are on the same scale. Patterning information was set in a script file. Depth was calibrated using an FEI Si materials file. Milling depth was set to 10, 25 and 50 nm respectively, which would approximately have been correct for silicon. Beam current was 87 pA. The magnification that was used during FIB milling was 10000 \times .

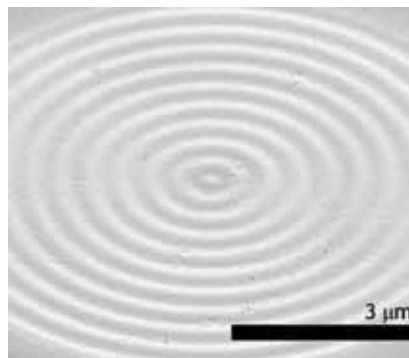


Figure 2.7: The single crystal substrate allows for precise depth variations, for example in this pattern, that was made using a BMP containing sinusoidally varying pixel values. This pattern was made using a 1000 pixel wide BMP file. Dwell time was 20 μs per pixel. The milling process was monitored using the SEM and stopped after an unknown number of passes.

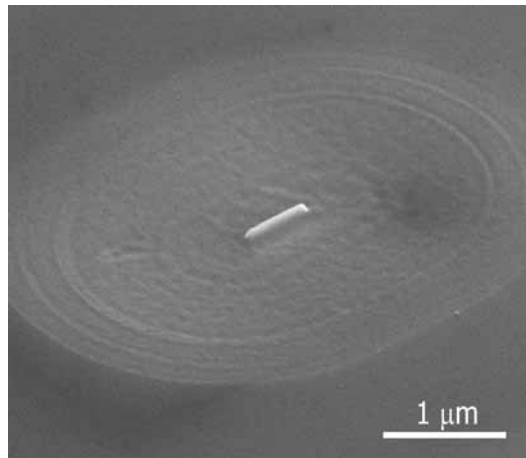


Figure 2.8: A single gold crystal nanorod (a so-called subtract wire) fabricated by removing the material around it. The pattern information was set in a BMP file. Milling was performed with 4 μs per pixel in 40 passes using a 10 pA beam current.

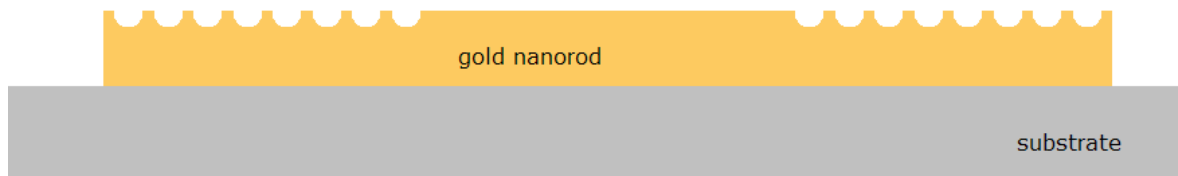


Figure 2.9: Schematic of a gold nanorod with a grating.

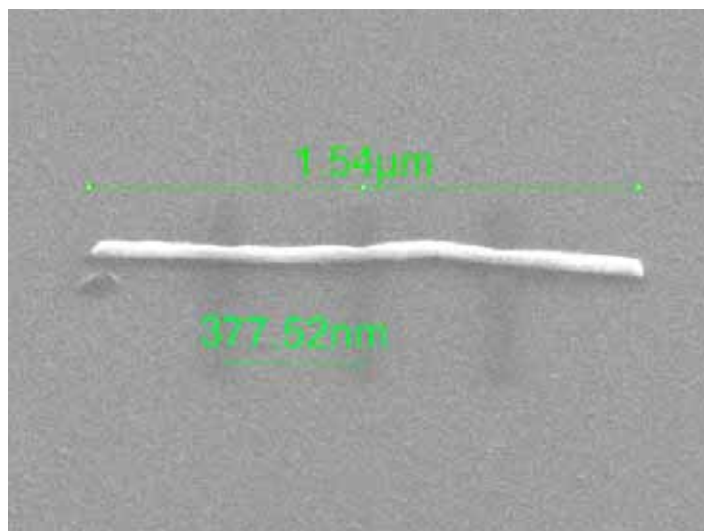


Figure 2.10: Short template-grown gold nanorod rod on silicon. The dark vertical lines show the location of FIB milling. The wire is thinner at the position of these lines.

The dissolved nanorods were deposited onto a heavily doped silicon substrate. The conductivity of this substrate avoided charging problems in both FIB and SEM.

Using SEM imaging, isolated rods were located. Aligning the ion beam was impossible in scanning ion imaging mode, because the milling rate on the rods was very high. A very precise alignment between electron and ion beam had to be performed to accurately position patterns on the rods.

For these rods we used a beam current of 10 pA.

On 1–5 μm long rods with 60 nm diameter 3–4 grooves with a Gaussian shape and a width of ~ 40 –50 nm were patterned. The groove pitch was varied between 200 and 380 nm on different rods.

Figure 2.10 shows a SEM images of a patterned wire (\varnothing 60 nm). These results confirm that even on very thin wires it is possible to make smooth and regular indentations.

The longer rods (5–15 μm) could be patterned with a longer series of grooves (pitch 250–500 nm), essentially a grating.

The spacing between the gratings at the ends of the wire was 7 to 16 periods, depending on the length of the wire.

2.2.4 Patterning of an evaporated gold film on quartz

A thin gold film was deposited onto a fused silica substrate with LN-cooled, argon ion assisted evaporation in an e-beam evaporator, by Martin Kuttge.

Charging as a result of the silica substrate makes using the FIB more difficult on these samples. In contrast with the single crystal gold, the silica is non-conductive. FIB milling is now possible, but care has to be taken to avoid charging of the gold layer. This can be done by grounding using

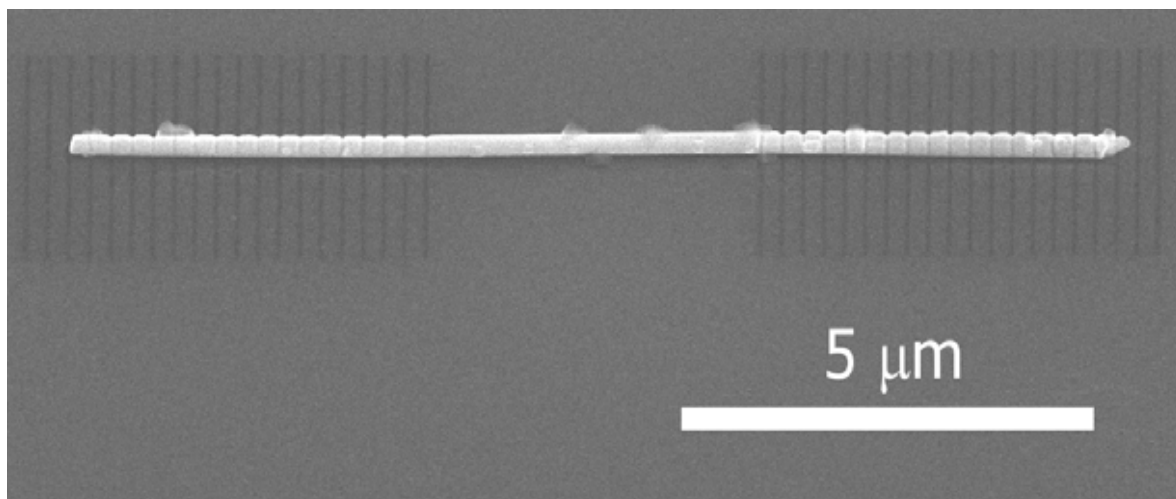


Figure 2.11: A gold nanorod with two gratings on a silicon substrate. The FIB milling area can be seen as dark lines on the substrate.

silver glue. Figure 2.12 shows an example in which the FIB was used to mill a grating in a thin gold film that would reveal the silica substrate.

2.2.5 Sample analysis

Au-shell colloids

Silica-core gold shell colloids, coated with a 40nm silica layer, were deformed into oblate ellipsoids by MeV ion irradiation [27] on a silicon substrate, performed by Joan Penninkhof.

It was unknown what the ion induced deformation would do to the gold layer. We used FIB to prepare the sample for a measurement of gold layer thickness by making a cross-cut of a particle (figure 2.13).

This was done by milling away one half of the bead. In this case it is not important to mill a perfect box, but the cut through the bead should be flat and uncontaminated. This is done by scanning the FIB in a transverse line, some distance away from the bead, slowly moving towards its center. The cut surface is always 'fresh' and has virtually no backspattering contaminations.

The results show that it is very well possible to make such a cut through these beads. The transparency in the images is caused by the high acceleration voltage of the electron beam, which is 30 kV. These images allow us to make a very rough estimate of the gold layer thickness, but the transparency and the moderate angle to the cut prevent an accurate measurement.

Additional SEM imaging with higher tilt and lower acceleration voltage are necessary to gain a better view of the cut and allow for a more precise thickness measurement.

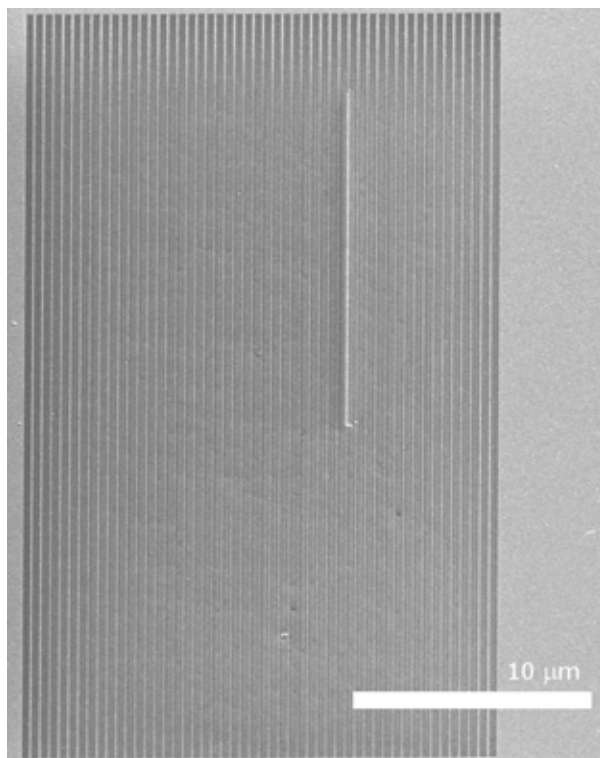


Figure 2.12: A grating on a 30 nm thick gold film on a silica substrate. The dark lines show the substrate; only thin strips of gold remain in between. The bright line in the center is a strip of gold that is not connected to the rest of the film. It is brighter because of charging due to the SEM electron beam.

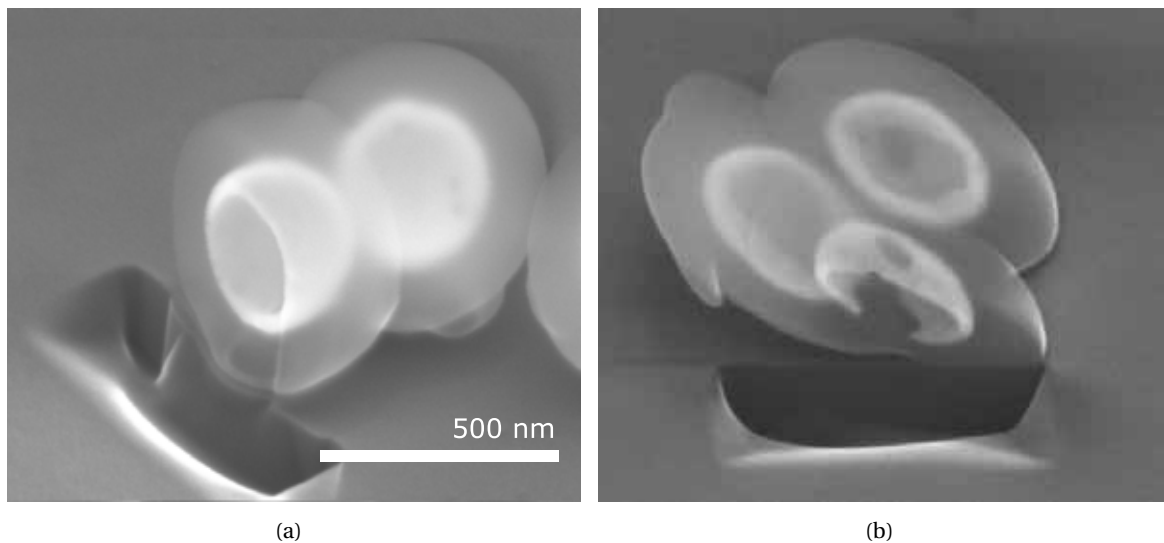


Figure 2.13: Beads before (a) and after (b) ion beam deformation that have both undergone FIB milling. It can be seen that at 30kV the beads are rather transparent for electrons. FIB milling revealed a cut through the wires to allow for a precise measurement of the gold layer thickness.

Chapter 3

FDTD simulations of gold nanorods

This chapter describes the finite-difference time-domain (FDTD) [28] simulations that we performed to acquire insight into the electric field intensity distributions on and around resonating gold nanowires for comparison with experimental results.

3.1 Methods

Structure design, simulation, and most analysis was done with MaFIA [29], a commercial FDTD package.

For excitation of a broad spectrum of modes we made use of a ringdown method [30]. In this technique a low-frequency plane wave excitation is imposed on a predefined structure. Scattering from discontinuities in the structure leads to the excitation of plasmonic modes. In a second step, the structure is allowed to 'ring down' and only resonant oscillations will remain. Analysis of the electric field in the ring down phase yields the frequencies that are resonant with the investigated structure.

The electric fields as a function of time around the structure are studied when excited at different resonance frequencies that can be learned from the ringdown. This shows the electric field distribution for every mode.

We investigated a gold cylinder, suspended in vacuo in the center of a box of $2 \times 1 \times 1 \mu\text{m}^3$ or

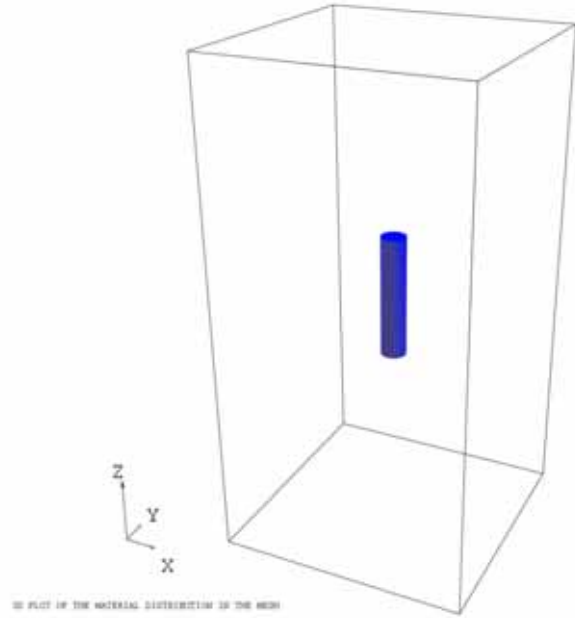


Figure 3.1: Model of the nanowire, as used in MaFIA. The gold nanorod is represented by a 500 nm long, 100 nm diameter cylinder.

attached to a gold substrate in a larger box ($4 \times 4 \times 3 \mu\text{m}^3$). We used 2 and 3 million grid cells, respectively.

Length and diameter of the wire were 500 and 100 nm, respectively. Figure 3.1 shows this configuration.

The electric field strength is monitored at several points along the wire and at its center.

The material parameters of the gold were modeled with the Drude model (equation 3.1). We used $\epsilon_{\text{static}} = 2.0$, $\epsilon_{\text{high}} = 1.0$, $\omega_{\text{plasma}} = 1.08 \cdot 10^{15}$ Hz, $\nu_{\text{collision}} = 4 \cdot 10^{13}$ rad/s.

$$\epsilon_r = \epsilon_h - \frac{(\epsilon_s - \epsilon_h)\omega_p^2}{\omega^2 - i\omega\nu_c} \quad (3.1)$$

3.2 Results

3.2.1 500 nm nanorod

Figure 3.2a shows the z -component of the electric field (pointing along the wire) at a point on the cylinder at the rod center during ringdown after excitation at 200 THz ($\equiv 1.5 \mu\text{m}$). The plane wave k -vector was perpendicular to the wire axis. A snapshot of the electric field distribution for this geometry is shown in figure 3.3a. The Fourier spectrum of the ringdown is shown in figure 3.2b.

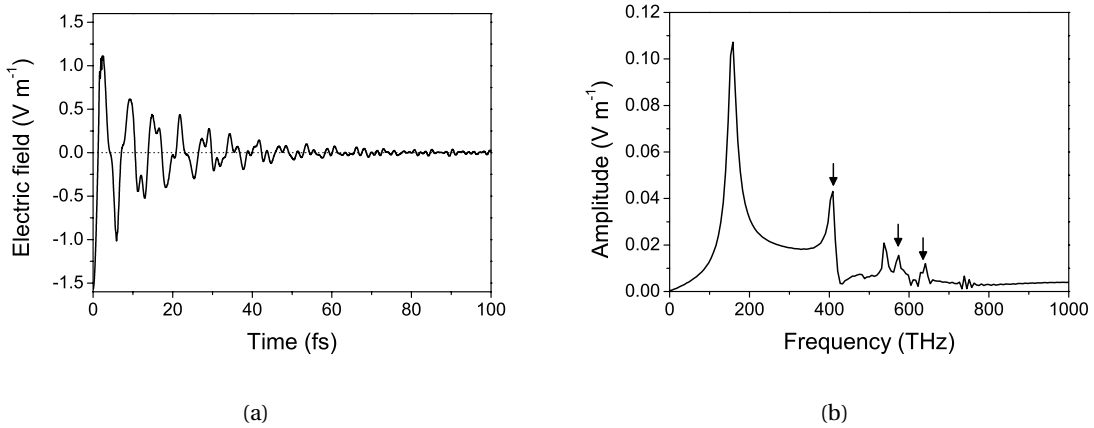


Figure 3.2: (a) z -component (along the wire) of the electric field during ringdown of the nanorod in vacuo after 200THz excitation, monitored at a point located on the surface of the rod at the rod center. (b) Fourier spectrum of this signal, showing the resonant frequencies. Peaks at 400 THz (749 nm), 575 THz (521 nm) and 620 THz (484 nm) are indicated by arrows.

Resonant peaks can be distinguished. Three prominent frequencies are 400 THz, 575 THz and 620 THz, indicated by arrows in the figure. In figure 3.4 we compare electric field snapshots along the wire at these different resonance frequencies.

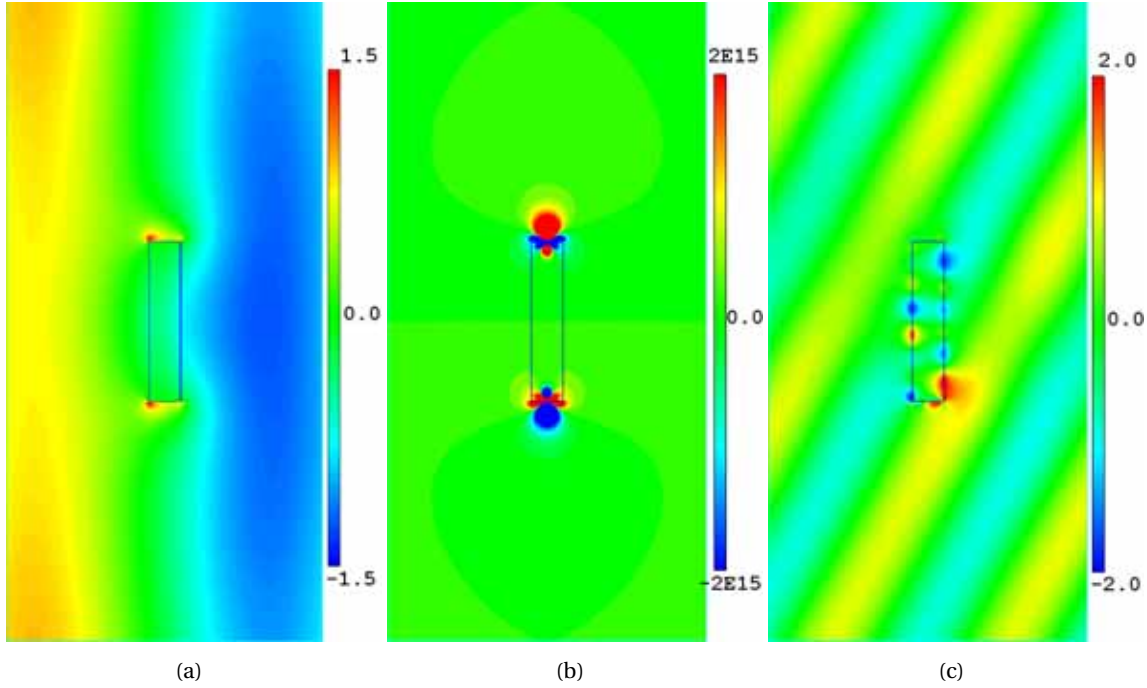


Figure 3.3: Three different ways of wire excitation. Colors represent electric field component in vertical direction. (a) A plane wave is incident from the left, having its wave vector perpendicular to the wire axis and polarization parallel to the wire axis. (b) Two dipoles excite modes with opposite electric fields on the wire ends. Dipoles are aligned with the wire axis. (c) A plane wave incident under an angle such that there is 180° phase difference on the wire ends. Polarization is along the blue and yellow bands in the image.

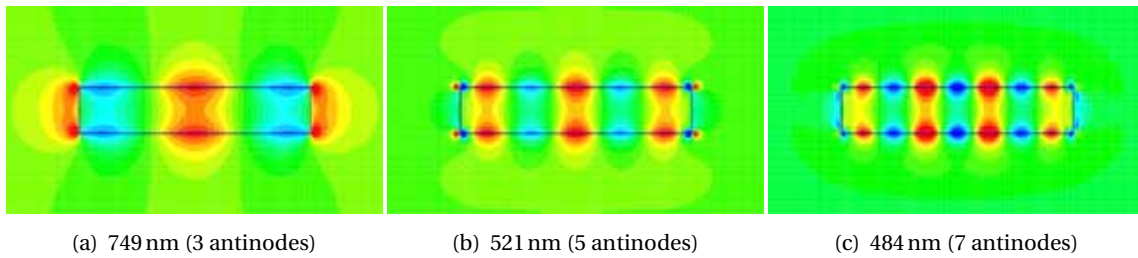


Figure 3.4: Snapshots of the z -component of the electric field (direction along the wire) in a plane through a gold nanowire of 500 nm length and 100 nm diameter. The wire was excited using a plane wave with direction inside the paper and polarization along the wire axis at different wavelengths that are indicated in the figure. Green indicates zero field, red and blue correspond to right and left pointing fields, respectively. These images show that after excitation an odd number of field antinodes appears on the wire.

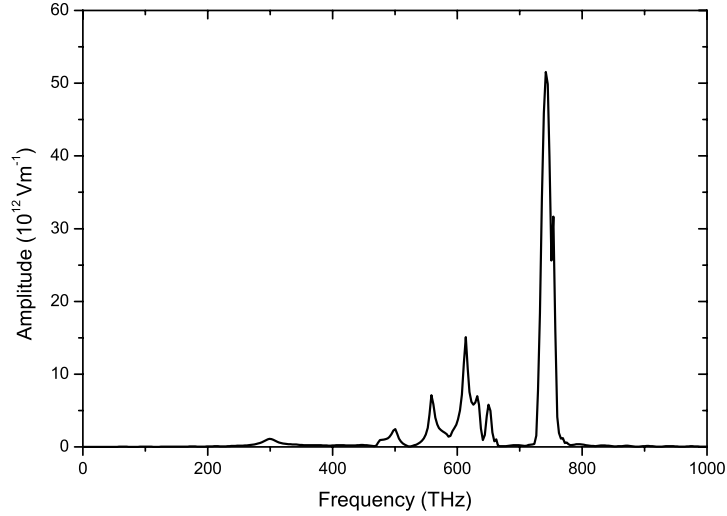


Figure 3.5: Ringdown spectrum after dipole method excitation. This graph shows the Fourier spectrum z -component of the electric field monitored at a point located on the surface of the rod at the rod center. The graph shows that other peaks appear than in the plane wave ringdown spectrum (see figure 3.2), which are attributed to modes with even number of antinodes on the wire.

For excitation with k perpendicular to the wire axis we only find modes that have an odd number of electric field antinodes. Based on symmetry arguments this implies that the field has equal direction at the wire ends. It is however expected that also modes with even number of antinodes exist [12], and that have opposite field direction at the ends. The plane wave that was used for the excitation part of the ringdown procedure had equal phase at both wire ends and is not expected to excite these modes efficiently, if at all.

We used two dipoles that oscillated at 200 THz with a 180° phase difference at the wire ends to excite modes with even number of antinodes. An electric field snapshot of this excitation configuration is shown in figure 3.3b. After this excitation we let the system ring down again. This ringdown was again monitored near the wire center. The Fourier spectrum of the z -component of this field is shown in figure 3.5.

The resonance spectrum derived from this ringdown yields resonances that are different than those in figure 3.2. The modes that were found with the dipole excitation method were subsequently excited at their resonance frequencies using plane wave excitation according to figure 3.3c with a tilted plane wave, such that the field at the ends of the rod had opposite direction (figure 3.3c). The tilt angle was thus frequency dependent.

Figure 3.6 shows snapshots of electric field profiles of these modes with even number of antinodes.

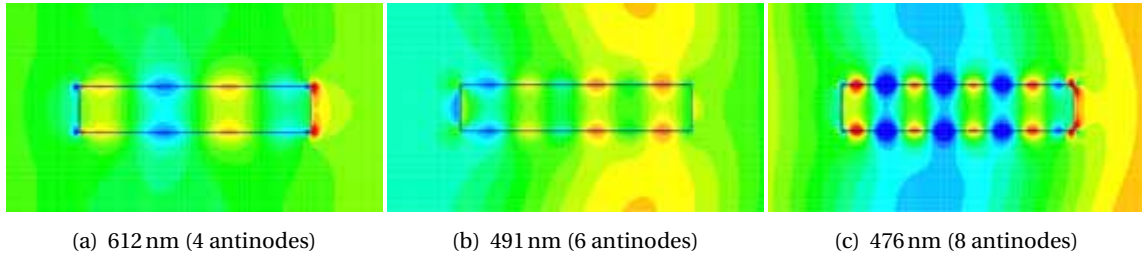


Figure 3.6: Snapshots of the z -component of the electric field (direction along the wire) in a plane through a gold nanowire of 500nm length and 100nm diameter, showing an even number of antinodes on the wire. The wire was excited using a plane wave not perpendicular to the image plane, but tilted over a certain angle in order for the wire ends to have a 180° phase difference. Excitation was at different wavelengths indicated in the figure. Green indicates zero field, red and blue correspond to right and left pointing fields, respectively.

To each mode we assign a spatial frequency k from the number of antinodes n and the wire length l according to $k = \pi n / l$ [12]. To set this relation, we assume that the resonances we observe are found for cases where two travelling plasmon waves on the rod travel in opposite direction and reflect at the wire ends. No phase shift at the reflecting ends is assumed.

Figure 3.7 shows the mode frequency as a function of the corresponding spatial frequency k , i.e. a dispersion relation for wire modes. The number of antinodes is indicated at each data point. The plot also contains the theoretical dispersion of a gold film using the same Drude model parameters as for the wires, and the light line in vacuum. The graph shows that the modes that are present on the wire have larger k than the surface plasmons on the planar film of the same frequency.

At 300 THz we do observe a small resonance in the ringdown (see figure 3.5), but using plane wave excitation this mode cannot be excited even at large angle. Interpolation of the dispersion relation suggests that this frequency corresponds to the mode with 2 antinodes.

3.2.2 Transverse resonances

Next to modes that are equivalent to plasmons propagating in the wire direction, which we will call longitudinal modes, there are so-called transverse modes, which correspond to plasmons that propagate perpendicular to the wire axis. We are mostly interested in the longitudinal modes, but we also did a simulation that gives information on these modes.

First we look again at the ringdown of the 500 nm nanowire, but we look at a different position and at a different field component. The black line in figure 3.8 shows the Fourier spectrum of the x -component of the electric field, which is perpendicular to the wire, monitored at the wire end. At the wire end we can monitor the effect of the longitudinal modes (with e -field along the wire, i.e. along the z -axis) in the x -component of the field because the wire end scatters. As a consequence we still see the peaks that were present in the ringdown in figure 3.2b in the ringdown spectrum of figure 3.8. In addition we see peaks at higher frequency than the asymptote in figure 3.7. We

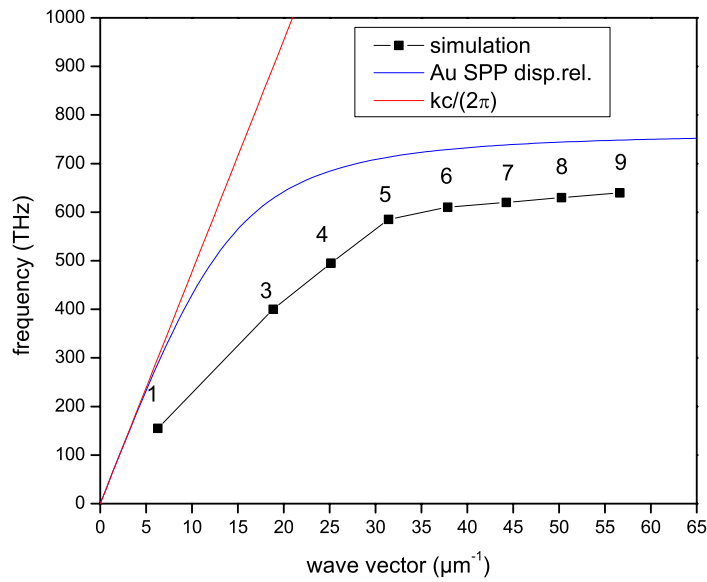


Figure 3.7: Dispersion of gold nanowire modes (numbered dots) determined from electric field distributions taken at characteristic resonance frequencies. Spatial frequency was determined by dividing the wire length by the number of maxima on the wire. The blue line shows the dispersion relation for a planar gold film. The graph shows that the wire resonances have a shorter wavelength than planar SPPs. The light line in vacuum is plotted in red.

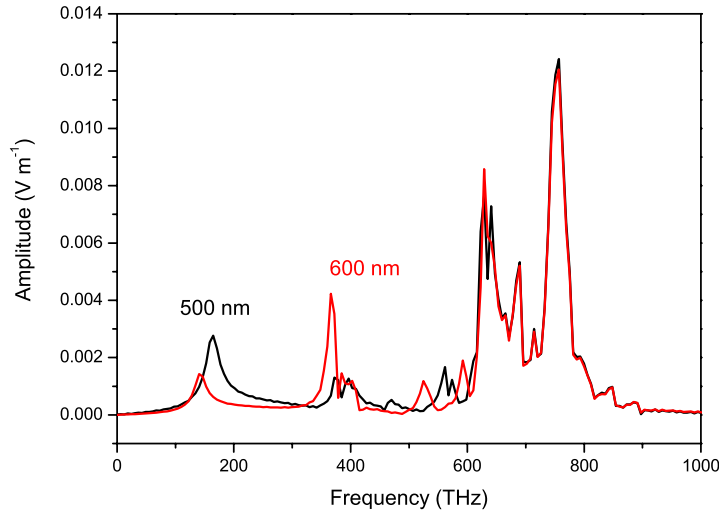


Figure 3.8: Ringdown comparison between 500 nm and 600 nm long wire. Shown is the Fourier spectrum of the x -component of the electric field, monitored at the wire end.

attribute these peaks to transverse resonances.

We performed another wire ringdown simulation with as only difference an increased wire length of 600 nm. The Fourier spectrum of this ringdown, of which we also monitored the x -component at the wire end, is plotted in figure 3.8 as a red line.

In this ringdown spectrum, the high-frequency peaks do not change as the wire length increases, but the lower-frequency peaks all redshift. This distinguishes the transverse from the longitudinal resonances, because the former are not dependent of wire length but the latter are.

3.2.3 Subtract-rod

Finally we simulated a gold nanorod on top of a gold substrate as a model of the FIB sample shown in figure 2.8. Figure 3.9a shows the geometry in MaFIA. The gold substrate was modeled by a $3\text{ }\mu\text{m}$ wide block that almost filled the simulation box.

Also on this structure we used the ringdown technique to excite modes. Figure 3.9 shows an electric field snapshot during plane wave illumination at 450 THz, one of the ringdown peaks.

We performed this simulation to show that this structure also shows plasmonic modes. We did not do a complete simulation of this structure, because in most cases the driving incoming wave sets the whole structure to an oscillation, which complicates identification of resonances that originate only from the wire.

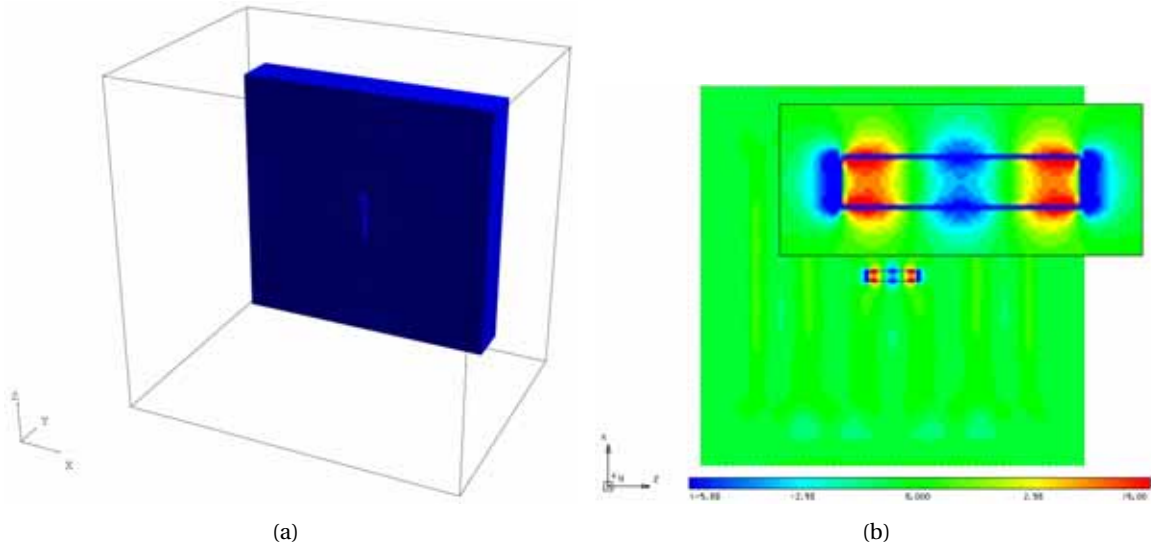


Figure 3.9: (a) The subtract-rod configuration. A $4 \times 4 \times 3 \mu\text{m}$ box with a gold slab on which a 500 nm long wire is positioned. (b) Snapshot of the z -component of the electric field around this structure at 450 THz. In this case, the plane wave direction is inside the paper and the polarization is horizontal. On the wire the antinodes of a standing wave can be distinguished, similar to the wires that were shown before. Inset: enlargement of the wire area.

3.3 Conclusions

These results show that the resonant behaviour of gold nanorods can be studied using FDTD. We showed that a wire can support multiple resonances in the visible. The modal electric field is strongly modulated in a node pattern along the rod.

It has also been shown that the dispersion curve for the resonances on the wire substantially differs from dispersion relation for the semi-infinite gold-vacuum interface SPP.

The electric field snapshots give us a qualitative idea of the geometrical properties of a wire resonance. The simulations presented here lack incorporation of a silicon substrate that usually supports the rods. This would be a next step in future work. In addition, a determination and implementation of optimal Drude parameters would allow for more quantitative statements about the resonance frequencies we expect in experiments.

Chapter 4

Cathodoluminescence measurements on plasmonic nanostructures

4.1 Introduction

This chapter reports on the measurements of cathodoluminescence (CL) signal on gold nanowires and annular structures upon irradiating these structures with a 30 kV electron beam. A modulated intensity profile along the nanowire, as seen in FDTD experiments, was indeed observed in experiment. This shows that CL is able to map the field distribution of plasmon modes in metal nanowires.

4.2 Setup

The setup we used for CL measurements is a FEI XL30 SEM in combination with a Gatan CL system. Figure 4.1 shows how luminescence generated by the electron beam is collected by a paraboloidal aluminum mirror that sends a collimated beam into a spectrometer. The mirror focus on the sample is $\sim 50\text{ }\mu\text{m}$ in diameter at a SEM working distance of 12.4 mm. The spectrometer is part of the Gatan system and uses a 150 lines mm^{-1} grating and a Princeton Instruments Pixis:100F CCD detector with a 1340×100 pixel array. The signal was obtained by binning over the 100 pixel width of the CCD.

The system uses a software package called Digital Micrograph, that communicates with the detectors and controls the scanning of electron beam. We have used it to scan the electron beam either in a 2D grid or on a series of spots on a single line, during which for each pixel a full spectrum is collected on the CCD. We call these acquisition modes spectral image and line scan, respectively.

All measurements presented here were background subtracted by subtracting an average over a few pixels for which the e-beam was dwelling on the substrate. We also corrected for CCD sensitivity. The grating efficiency was not known so it was not taken into account.

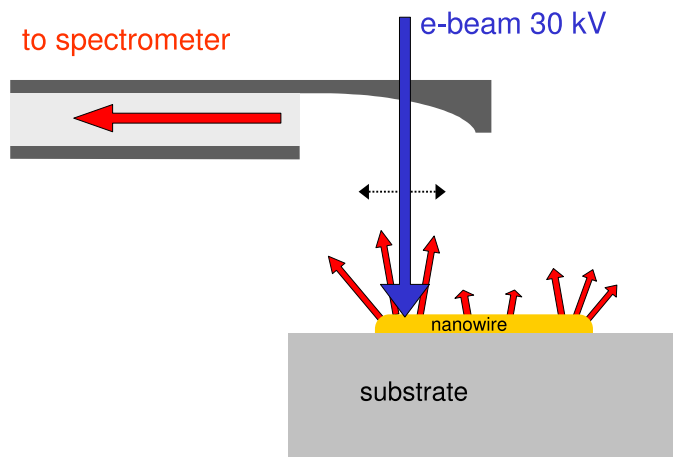


Figure 4.1: CL collection configuration. The electron beam falls through a hole in the paraboloidal mirror. Light generated by the e-beam is collected by the mirror, which has a $\sim 50\ \mu\text{m}$ focus on the sample. It has a large collection angle ($\sim 90^\circ$ in both directions). The light guide on the left guides a parallel beam into the spectrometer.

4.3 CL measurements on gold nanorods

4.3.1 E-beam and lift-off nanorods

This section describes CL measurements of gold nanorods that were fabricated on a heavily doped silicon substrate using e-beam lithography, evaporation and lift-off (figure 4.2). The nanorod lengths range from 300 to 1200 nm; their width is 100 to 200 nm and they are 80 nm high. As estimated from the SEM image, the grain size is ~ 20 nm. The polycrystallinity implies grain boundaries and roughness that may scatter surface plasmons. We do not expect absorption caused by impurities, because the gold that is deposited by evaporation is very pure.

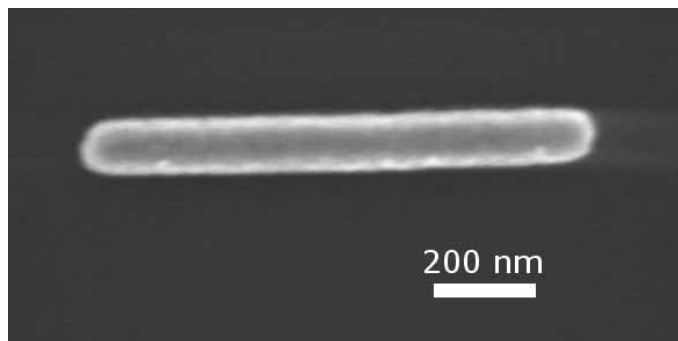


Figure 4.2: SEM image of gold nanorod on silicon, made by e-beam lithography and lift-off. Width is 100 nm, length 1000 nm

The conductivity of the substrate prevents from charging by the electron beam. It does contribute to the background CL signal, however.

Figure 4.3 shows results from spectral images for 750nm and 1200nm long rods. Data are shown at 583 nm and 662 nm for the 750 nm long rod and at 495 nm, 580 nm and 710 nm for the 1200 nm long rod. When the electron beam dwells at the rod ends, more light is produced. This occurs at all wavelengths. As a function of wavelength several periodically distributed nodes and antinodes are found inside the wires. A quick estimate of the distance between adjacent maxima gives values close to $\lambda/2$ in each case, where λ is the vacuum wavelength, which suggests that we are looking at optical resonances. In the following we will further investigate these resonance effects.

Figure 4.3c is a spectral image at 495 nm. Light is mostly generated when the electron beam dwells at the wire edge, which causes the outline in the image. It is not clear what phenomenon causes this signal. It suggests a resonance that corresponds to a wave propagating perpendicular to the wire axis, but that does not explain the high signal that is still present at the tips of the rod. This CL profile deserves further investigation, but we will focus on the maxima in the wire.

Line scans along the wire axis are a good way to measure the profile along the wire in more detail. CL acquisition time is often limited by drift of the stage relative to the electron beam or vice versa (for instance, figure 4.3a and b suggest that the wire moved to the left bottom during measurement). A single line scan is relatively fast, which allows for a longer dwell time as well as smaller pixels, i.e. a higher spatial resolution, and at the same time is less sensitive to drift than a spectral image.

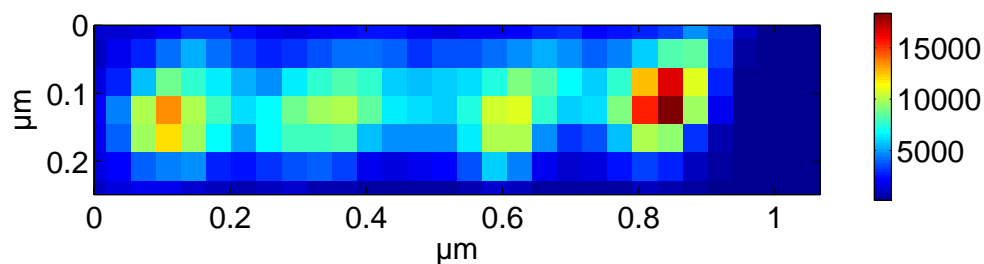
Figure 4.4 shows the spectral data for a line scan along the 750nm long gold wire of which two-dimensional images are shown in figure 4.3a and b. The spectral axis is shown horizontally, the spatial axis vertically. The rod position is indicated by the white vertical line.

Figure 4.5 shows vertical cuts through this figure at 520 nm, 583 nm and 662 nm: spatial profiles of a spectral component along the wire. The line traces in figure 4.5 show that clearly three modes are excited: at ~660 nm three maxima are observed; at ~590 nm four maxima, and at ~520 nm five.

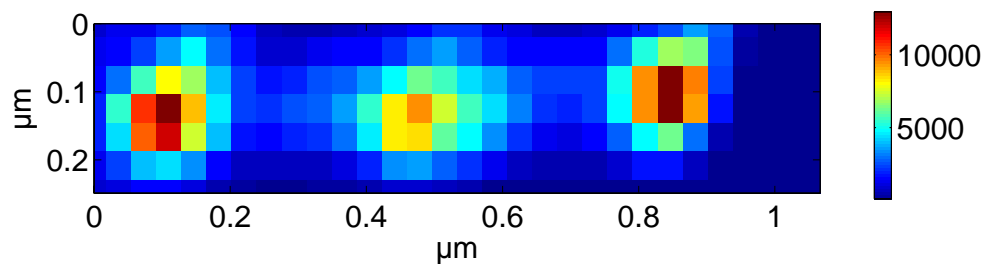
Figure 4.6 shows spectra at important positions on this line scan. The spectra vary substantially, which shows that multiple resonances contribute. The spectra also differ substantially in cases where we expect symmetry.

If we look for this asymmetry in other data we see that both figure 4.4 and 4.5 show that the right wire end produces more CL signal than the left end. This difference is present in every CL line trace of these nanorods and is not related to this particular wire. We attribute this to angle-dependent radiation of the wire in combination with angle dependent sensitivity in the detection system due to misalignment of the setup. We investigated this asymmetry further by subtracting the left-end spectrum from the right-end spectrum for a few wire line scans. Figure 4.7 shows two representative examples of these difference spectra. We defined the wire ends by the end peaks of a line trace taken at 600 nm. The facts that the difference peak has a more or less fixed position and that its shape is generally very similar to a single Gaussian peak, suggest that a single resonance might be responsible for the effect and that future measurements can clarify the origin of this resonance, for example using polarized detection.

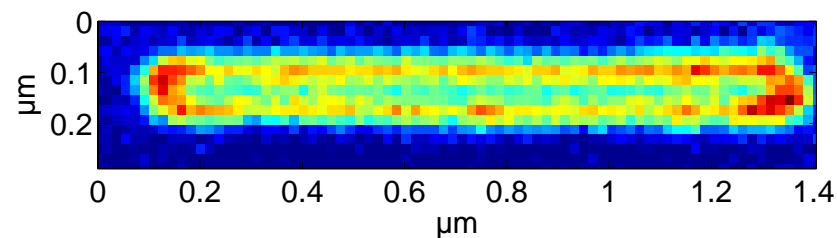
The wire end differences cause difficulty in determination of the mode spectrum. For example,



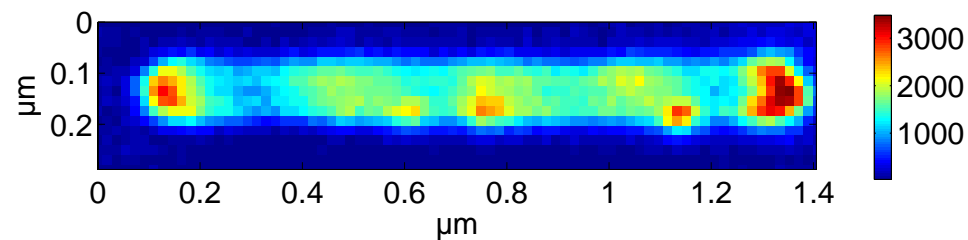
(a) 583 nm emission from a 750 nm nanorod



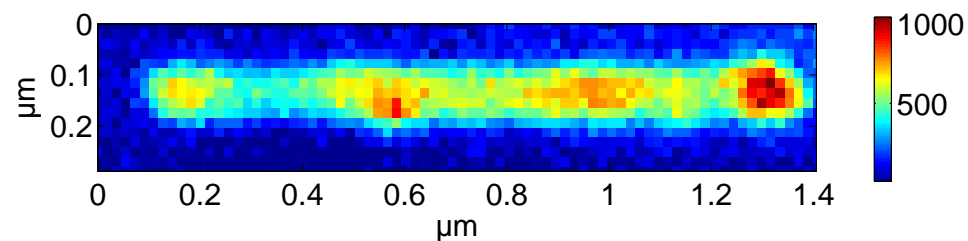
(b) 662 nm emission from a 750 nm nanorod



(c) 495 nm emission from a 1200 nm nanorod



(d) 580 nm emission from a 1200 nm nanorod



(e) 710 nm emission from a 1200 nm nanorod

Figure 4.3: Spectral CL images, all with a 10 nm bandwidth, of a gold nanorod on a silicon substrate made by e-beam lithography and lift-off. Nanowire length was 750 nm (a,b) and 1200 nm (c-e).

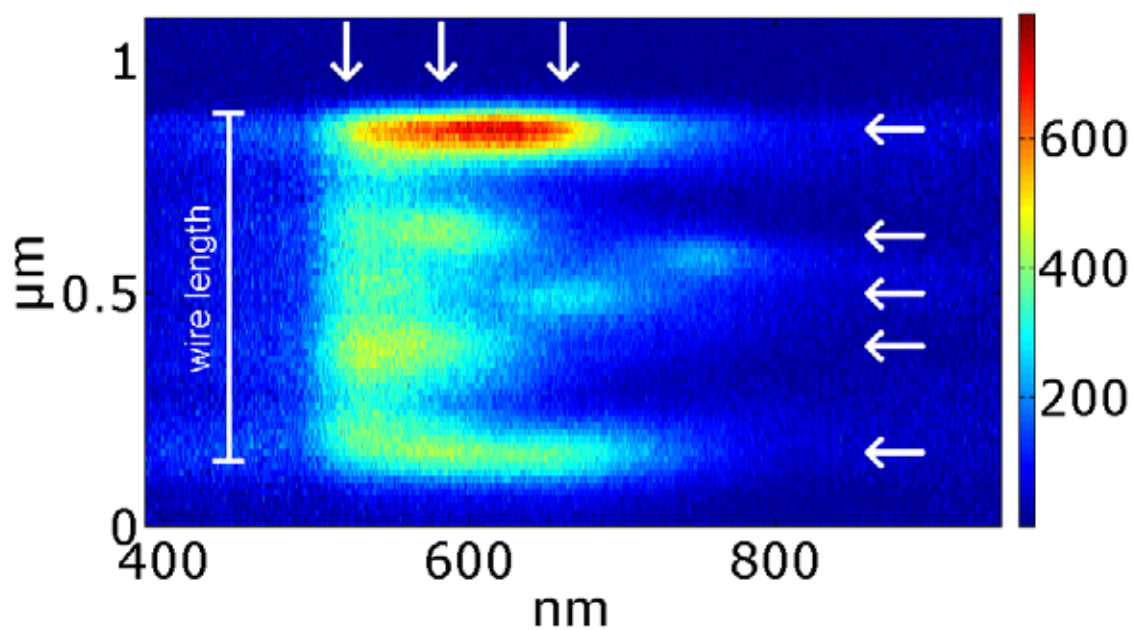


Figure 4.4: CL linescan through a 750 nm long gold nanorod fabricated with e-beam lithography. The spectral axis (resolution: 0.4 nm) is shown horizontally, the spatial axis vertically (resolution: 14 nm). The white bar indicates the size of the nanowire. The white arrows that point down correspond to the line traces in figure 4.5. The left-pointing arrows show the location of the spectra in figure 4.6.

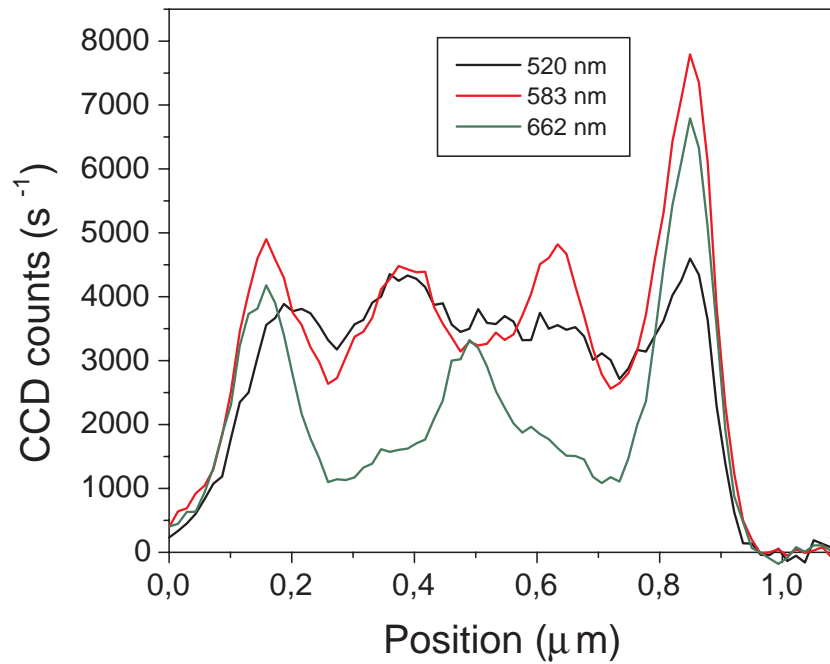


Figure 4.5: CL signal for wire of 750 nm length at 520, 583 and 662 nm detection wavelength (5 nm spectral bandwidth). Left in this graph corresponds to the bottom of figure 4.4.

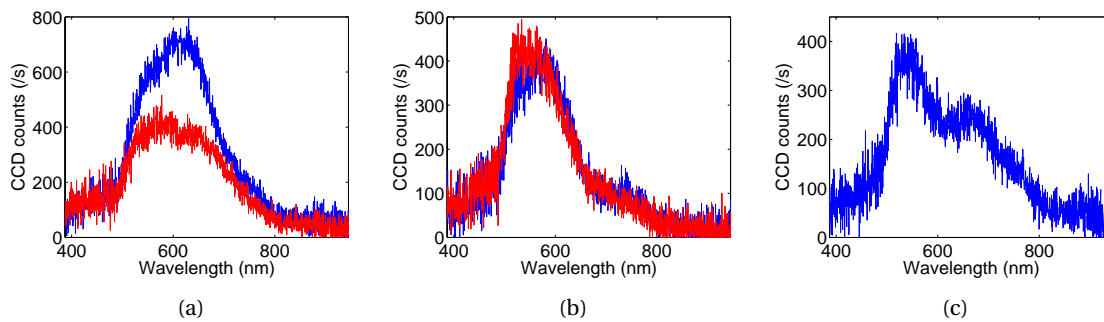


Figure 4.6: Horizontal line traces through figure 4.4, i.e. CL spectra at different positions along the wire. (a) Wire ends at 0.17 and 0.86 μm , (b) The two maxima inside the wires at 0.63 and 0.39 μm , (c) The center maximum at 0.51 μm .

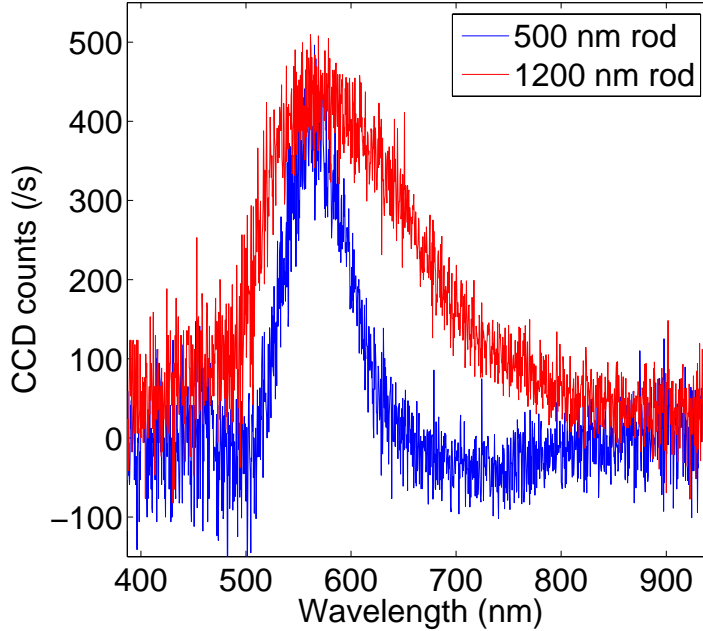


Figure 4.7: Spectral difference between CL signal from the right and the left end for a 500 nm and a 1200 nm rod, obtained by subtracting the left end spectrum from the right end spectrum. The close proximity of their center wavelength and their Gaussian shape suggest a common origin.

it is clear that a peak fit would give different results at the two wire ends for the spectra in figure 4.6.

Now we tried to find the mode frequencies by fitting spatial profiles to the line scan (figure 4.8). Spatial profiles were based on figure 4.5 and the profiles consisted of 3, 4 and 5 Gaussian peaks along the wire. We corrected the profiles using a wavelength-dependent asymmetry correction that was equal to the asymmetry that is present in a line scan. We determined the asymmetry ratio as a function of wavelength by dividing the right end spectrum by the left end spectrum.

The fit determined how the line profile at a certain location was best composed of the 3, 4, or 5 maxima basis elements.

The result of this fit is shown in figure 4.9. Here, three spectra are plotted that show the spectral position of each mode. Figure 4.9b is a reconstruction of the linescan data from the fit result. Note that the peaks in figure 4.9a overlap considerably and that they are not perfect Gaussians. This shows that our spatial input was not equal to the actual mode profiles. The decrease of mode wavelength with an increase of mode peaks on the wire is consistent with the organ pipe-model.

From the line traces (figure 4.5) as well as the fitted spectra (figure 4.9) a spatial wavelength and a mode wavelength can be determined. We calculated these values for the 750 nm long wire and a 500 nm long wire; the results are plotted in the dispersion relation in figure 4.10.

As a final remark on the data it is worth noticing that there is a spot in figure 4.4 at approximately 750 nm that was not reproduced in the fit. The offcenter position and the small width of the

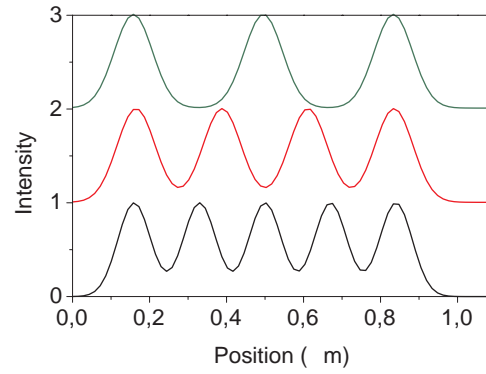
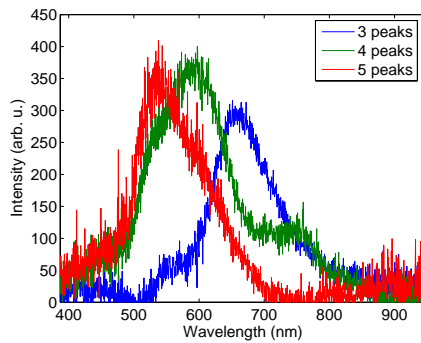
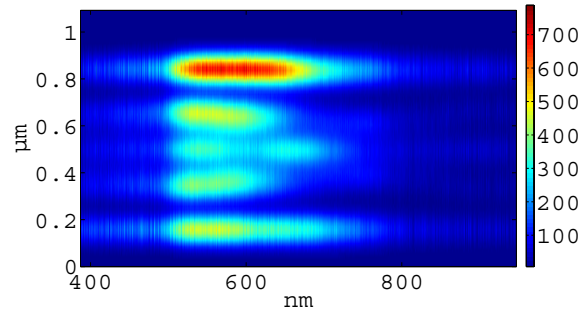


Figure 4.8: Spatial profiles that were fitted to the data in figure 4.4. The curves have been vertically shifted for clarity.



(a) The spectra that result from fitting the spatial profiles in figure 4.8 to the data in figure 4.4.



(b) Reconstruction of the line scan from the fit results

Figure 4.9: Analysis of the linescan (figure 4.4) by a spatial fit.

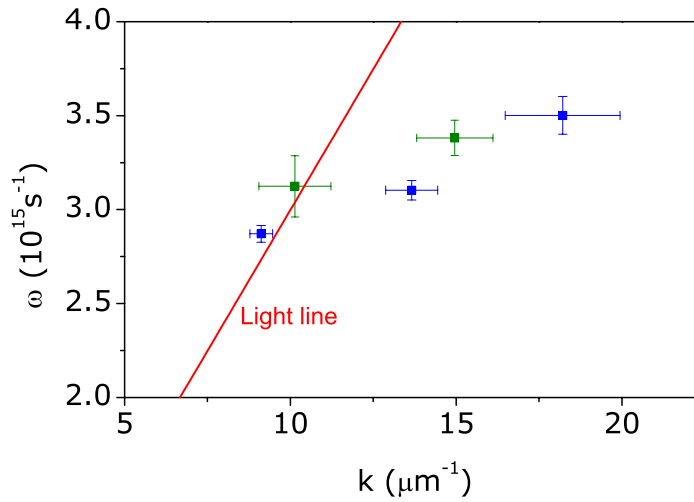


Figure 4.10: Dispersion plot of the rod resonances, for the 750 nm rod (blue) as well as a 500 nm rod (green) combined.

spot suggest this is a spurious signal caused by a wire irregularity. This is confirmed by the spectral image at this wavelength and a SEM picture, that both show a blob, off axis, near the center of the wire (figure 4.11). Other wires reproduce the mode maxima, but not this signal.

This section has shown that we are able to determine spectral and spatial properties of plasmonic modes on gold nanowires both during one measurement. Both the CL measurements and the FDTD simulations in the previous chapter show a modulation along the wire that is wavelength dependent. This confirms that the modal electric field is important in explaining the CL signal modulation.

Others have determined the local density of states (LDOS) around metal nanowires [21, 11] and it has been suggested that LDOS is also strongly related to CL excitation efficiency. The profiles we measured here do indeed resemble the LDOS profiles.

Future work will show which model is best suited to explain the results of CL measurements.

4.3.2 Subtracted rods

The CL behaviour of a subtracted rod (figure 2.8) was also investigated. This structure was fabricated using FIB (see section 2.2.2), and basically is composed of a golden ridge on a gold surface. Both the ridge and the rest of the surface were part of a single gold crystal. This sample provided a very straight rod (estimated roughness < 5 nm) with no irregularities. In addition, the surrounding of the rod also has a very low roughness. However, all of the surface on and around the wire will contain gallium contaminations as a result of the FIB milling, which might cause extra damping

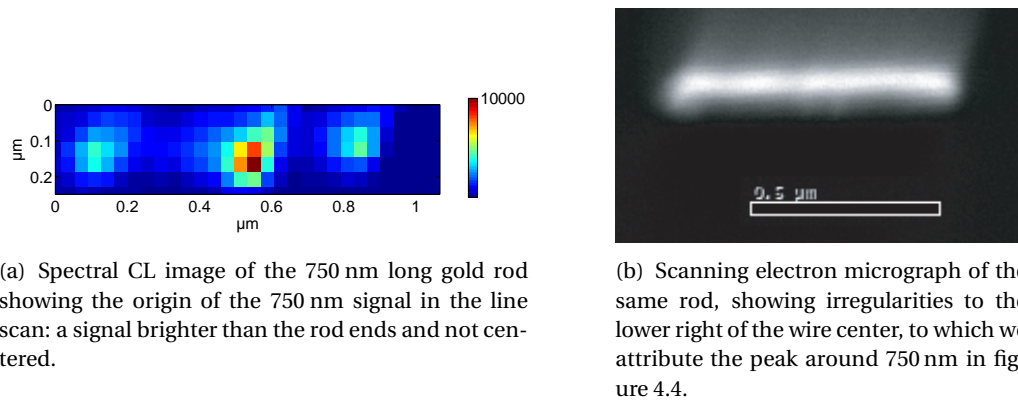


Figure 4.11

for the propagating plasmon modes.

The rod used in this experiment had a length of 560 nm and a height of approximately 100 nm. Around it, the material was removed, such that there should be no discontinuities in the surface surrounding the wire. However, the FIB milling induced some roughness.

We made a spectral CL image of the nanorod using 15 nm pixel spacing. The field of view was 210×720 nm. Three representations of this spectral data are shown in figure 4.12, using different detection wavelength windows.

Again, excitation at the wire ends always generates CL signal. We also see wavelength dependent features. In addition to the wire end signal, at 548 nm we see two maxima within the wire and at 595 nm there is one. Figure 4.13 shows line traces through spectral images in figure 4.12a and b that confirm that we see multiple peaks in spatial direction as a function of wavelength.

This section shows that also a golden ridge can behave like an isolated nanowire and support plasmonic resonances that can be mapped with CL.

4.3.3 Template grown nanorods

Other feasible candidates for CL mode observation are template grown, presumably single-crystal gold wires, shown in figure 4.14 and described in section 2.2.3. Their small roughness seems a big advantage in a stronger mode confinement and the possibility to see higher order modes on longer wires [10], because it reduces scattering from the wire and thus will lead to longer propagation length and clearer mode profiles.

The wires were dispersed onto a silicon substrate from a solution in ethanol. A disadvantage was that wires very easily aggregated, which caused only few single wires to be isolated from others. A second disadvantage was that the ethanol solution as well as the wires themselves contained impurities originating from the original template in which they were grown. A third disadvantage is that many rods were bent or had variations in the shape of their ends.

We have only done a few experiments with these wires. Figure 4.15 shows the SEM image of a

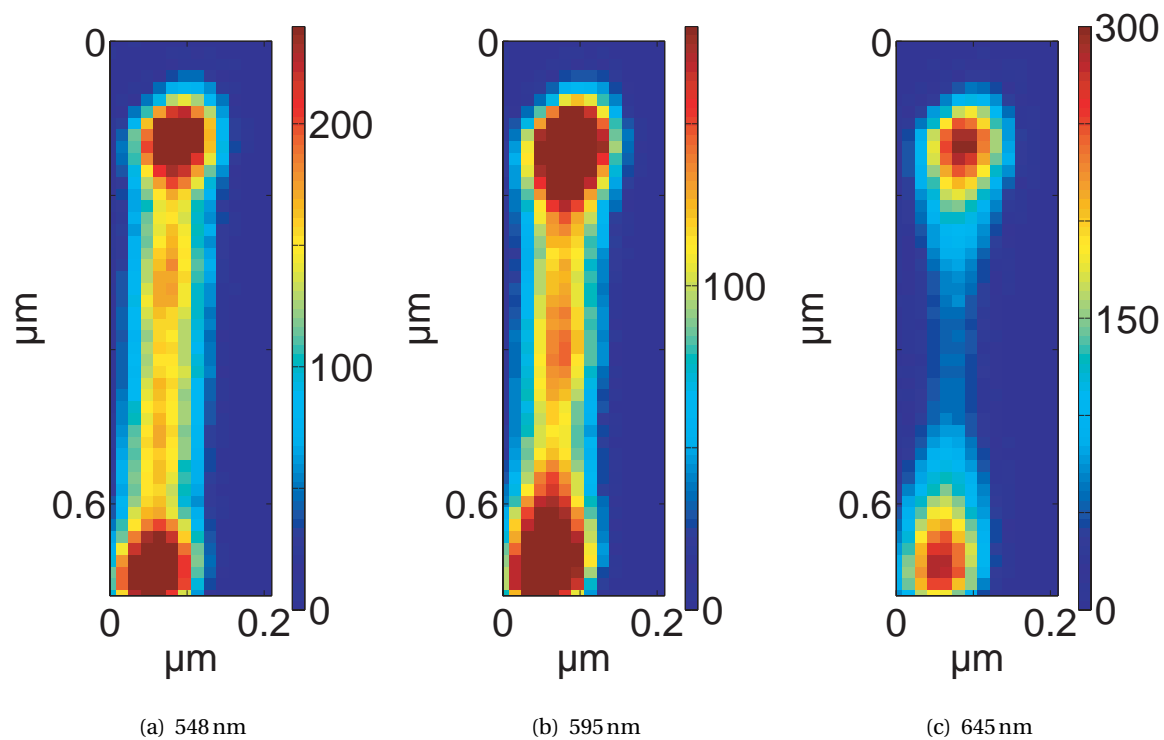


Figure 4.12: Spectral CL images (bandwidth 5 nm) corresponding to a 560 nm long and 100 nm wide subtracted nanorod. Note the two maxima (a) or one maximum (b) within the wire.

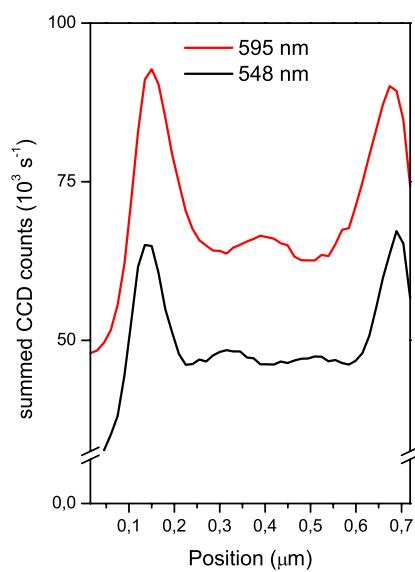


Figure 4.13: Line traces along the spectral image of the 560 nm long subtracted rod.

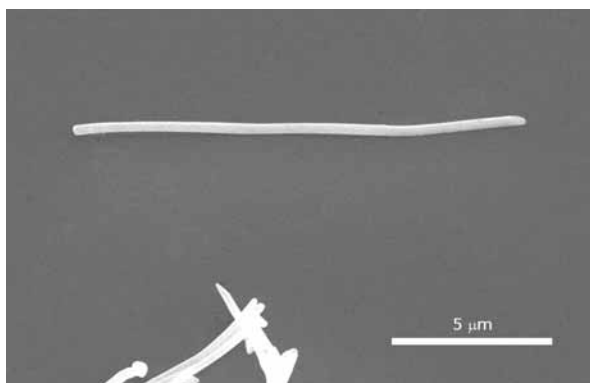


Figure 4.14: SEM image of a single crystal template-grown gold nanorod. An isolated specimen lies close to a cluster

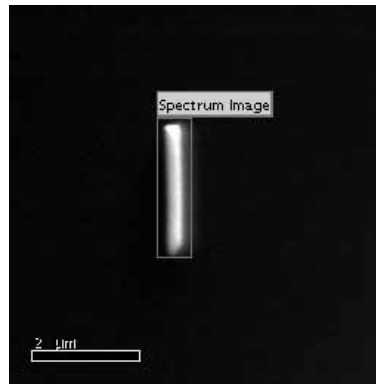


Figure 4.15: A 2.3 μm long and 300 nm wide single crystal gold rod. The CL scan box is also shown in this figure.

2.3 μm long and 300 nm wide gold nanorod that we used to measure the spectral image shown in figure 4.16. Similar to the e-beam fabricated wires, this wire has a strong CL signal at the wire ends, and several maxima within the wire.

Further experiments are necessary for a more in-depth analysis of mode behavior in these wires.

4.4 Annular nanoresonators in gold

As a result of the circular symmetry, annular structures are promising structures for confinement of plasmonic resonances on a metal surface. In this section we look into annular resonators that consist of one or multiple rings on a single crystal gold surface.

4.4.1 Single rings

In this experiment we studied rings with a radius ranging between 150 and 290 nm and depths of 100, 250 and 500 nm, fabricated using FIB (see figure 2.6). The rings are 10 μm apart, and we assume they do not influence each other. In the CL setup the electron beam was positioned in the center of a ring, and subsequently a spectrum was measured with the CCD detector during a period of 5 seconds.

The results are plotted in figure 4.17(a-c) for the three ring depths. In all cases strongly peaked spectra can be observed. For a single depth, resonance peaks redshift for larger ring diameter. This indicates that the peaks are due to resonant modes.

Comparing the data in figures 4.17(a-c) shows that groove depth has a large influence on the resonance frequencies.

In addition to the spectral shift, an overall decay in CL intensity is observed for larger rings. This shows that even on a 500 nm scale plasmon damping plays an important role.

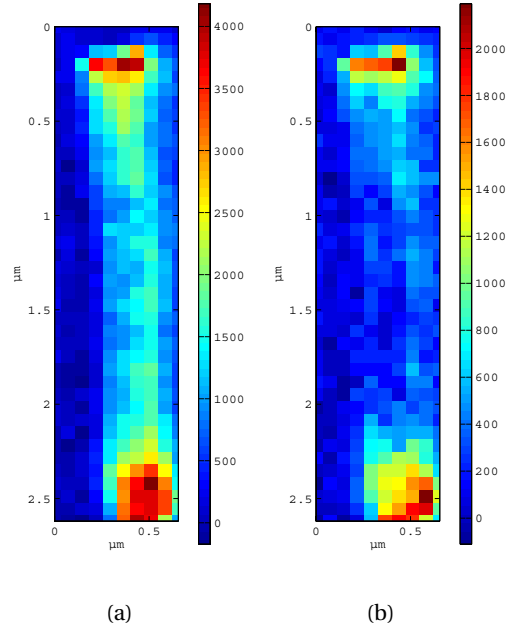


Figure 4.16: Spectral images at 683 and 770 nm of a template-grown nanorod (bandwidth 30 nm). The left figure shows that an profile is present in the wire, that has a period similar to $\lambda/2$ where λ is the vacuum detection wavelength.

4.4.2 Annular nanoresonators

It has been shown that annular resonators composed of multiple rings show mode behavior that can be linked to simulations [20]. In the FIB patterning of these rings in an evaporated silver film, differences in milling rate between adjacent crystal domains causes relatively great roughness in the grooves. This is a complication in the comparison of simulation with experiment. In general, it also limits the control over the groove shape.

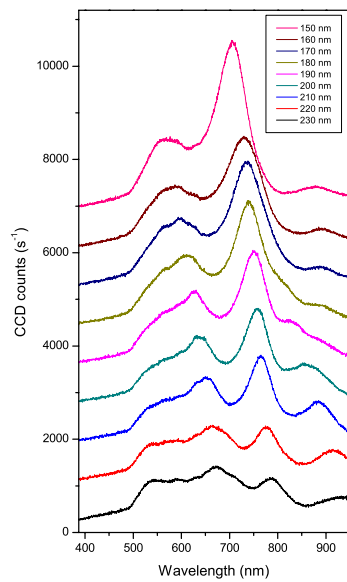
We used a single crystal gold surface, on which FIB milling does not suffer from grain differences. In addition, gold has better oxidation resistance. The great control that the FIB offers on this surface allowed us to pattern different groove profiles (see figure 2.7).

We verified the existence of mode behavior on this sample. Spectral CL images of an annular nanoresonator with 100 nm groove depth and 500 nm groove period are presented in figure 4.18.

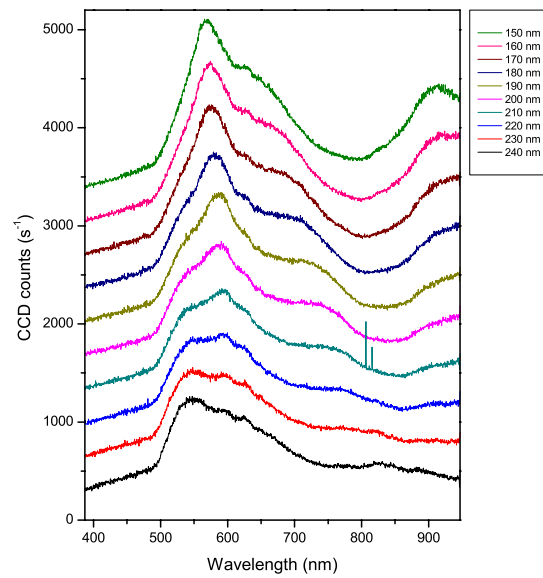
The ring profile gives a strong confirmation of such resonances.

4.5 Conclusions

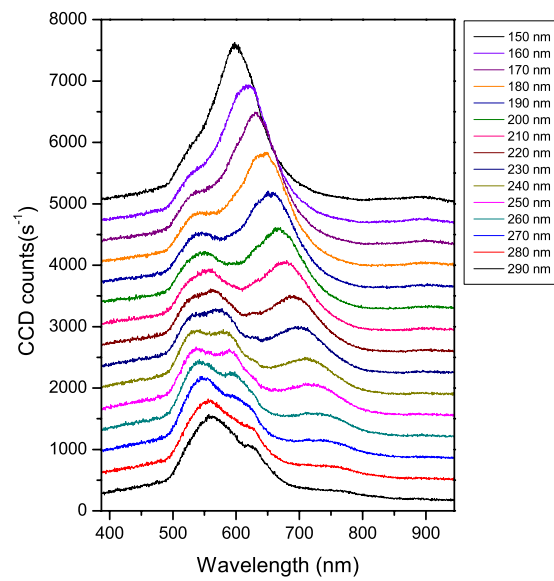
In this chapter we have shown that the cathodoluminescence imaging spectroscopy provides a precise spatial probe of plasmonic modes in metal nanostructures. A variety of samples has been shown to support plasmonic resonances of which the spatial and spectral properties can be re-



(a) ~500 nm deep

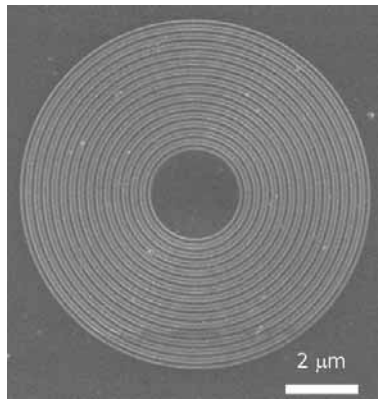
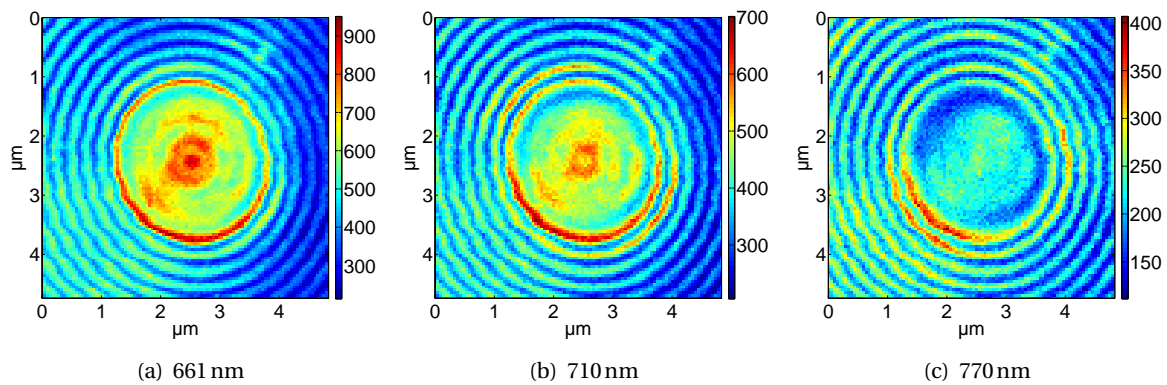


(b) ~250 nm deep

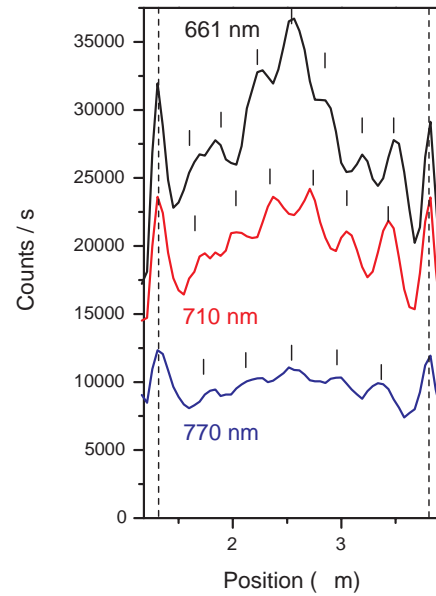


(c) ~100 nm deep

Figure 4.17: CL spectra for single ring-resonators in single crystal gold, with radius ranging between 150 and 290 nm, for different ring depths indicated in the figure.



(d) SEM image of the nanoresonator. The resonator center plateau has a $2.6 \mu\text{m}$ diameter. There are 15 grooves with 250 nm pitch and 100 nm depth.



(e) Line profiles through (a-c). This figure indicates a changing number of rings on the center plateau as the detection wavelength changes. The dashed lines denote the center plateau edge.

Figure 4.18: (a-c) Spectral images (5 nm bandwidth) at different detection wavelengths of the the annular nanoresonator (d). (e) Shows line traces through the spectral image.

solved with CL at a very high resolution.

In fact, each of these experiments shows a glimpse of the many phenomena for nanophotonics that cathodoluminescence can reveal, and it is clear that the technique is promising enough to start an in depth analysis of all its aspects.

We have shown that CL signal from gold nanowires is modulated along the wire axis with a wavelength dependent profile. These mode profiles qualitatively agree with the profiles that FDTD simulations give. Further measurements and simulations are necessary for a more quantitative comparison and to verify the dispersive properties of plasmonic modes on nanowires.

Although the results suggest that CL maps the spatial properties of modes present in the structure, it is not well understood how the process of electron impact is related to mode excitation efficiency, and it is important to gain more knowledge about the underlying mechanisms. Nanowires with an oscillating CL profile, as we have shown here, are promising structures that might give us this knowledge.

Bibliography

- [1] H. Raether. *Surface Plasmons*, volume 111. Springer, 1988.
- [2] William L. Barnes, Alain Dereux, and Thomas W. Ebbesen. Surface plasmon subwavelength optics. *Nature*, 424, 2003.
- [3] J.R. Krenn, H. Ditlbacher, G. Schider, A. Hohenau, A. Leitner, and F.R. Aussenegg. Surface plasmon micro- and nano-optics. *Journal of Microscopy*, 209, 2003.
- [4] Rashid Zia, Jon A. Schuller, Anu Chandran, and Mark L. Brongersma. Plasmonics: the next chip-scale technology. *Materials Today*, 9, 2006.
- [5] J.R. Krenn and J.-C. Weeber. Surface plasmon polaritons in metal stripes and wires. *Phil. Trans. R. Soc. Lond. A.*, 362, 2004.
- [6] J.R. Krenn, B. Lamprecht, H. Ditlbacher, G. Schider, M. Salerno, A. Leitner, and F.R. Aussenegg. Non-diffraction-limited light transport by gold nanowires. *Europhysics Letters*, 60, 2002.
- [7] Aric W. Sanders, David A. Routenberg, Benjamin J. Wiley, Younan Xia, Eric R. Dufresne, and Mark A. Reed. Observation of plasmon propagation, redirection, and fan-out in silver nanowires. *Nano Letters*, 6, 2006.
- [8] W.L. Schaich, G. Schider, J.R. Krenn, A. Leitner, F.R. Aussenegg, I. Puscasu, B. Monacelli, and G. Boreman. Optical resonances in periodic surface arrays of metallic patches. *Applied Optics*, 42, 2003.
- [9] J.R. Krenn, G. Schider, W. Rechberger, B. Lamprecht, A. Leitner, and F.R. Aussenegg. Design of multipolar plasmon excitations in silver nanoparticles. *Applied Physics Letters*, 77, 2000.
- [10] Harald Ditlbacher, Andreas Hohenau, Dieter Wagner, Uwe Kreibig, Michael Rogers, Ferdinand Hofer, Franz R. Aussenegg, and Joachim R. Krenn. Silver nanowires as surface plasmon resonators. *Physical Review Letters*, 95(25):257403, 2005.
- [11] Kohei Imura, Tetsuhiko Nagahara, and Hiromi Okamoto. Near-field optical imaging of plasmon modes in gold nanorods. *The Journal of Chemical Physics*, 122(15):154701, 2005.

- [12] G. Schider, J. R. Krenn, A. Hohenau, H. Ditlbacher, A. Leitner, F. R. Aussenegg, W. L. Schaich, I. Puscasu, B. Monacelli, and G. Boreman. Plasmon dispersion relation of au and ag nanowires. *Physical Review B (Condensed Matter and Materials Physics)*, 68(15):155427, 2003.
- [13] L. Billot, M. Lamy de la Chapelle, A.-S. Grimault, A. Vial, D. Barchiesi, J.-L. Bijeon, P.-M. Adam, and P. Royer. Surface enhanced raman scattering on gold nanowire arrays: Evidence of strong multipolar surface plasmon resonance enhancement. *Chemical Physics Letters*, 422, 2006.
- [14] P. Muhlschlegel, H.-J. Eisler, O.J.F. Martin, B. Hecht, and D.W. Pohl. Resonant optical antennas. *Science*, 308, 2005.
- [15] Detlef Heitmann. Radiative decay of surface plasmons excited by fast electrons on periodically modulated silver surfaces. *J. Phys. C: Solid State Phys.*, 10, 1977.
- [16] S. J. Smith and E. M. Purcell. Visible light from localized surface charges moving across a grating. *Phys. Rev.*, 92(4):1069, Nov 1953.
- [17] J.T. van Wijngaarden, E. Verhagen, A. Polman, C.E. Ross, H.J. Lezec, and H.A. Atwater. Direct imaging of propagation and damping of near-resonance surface plasmon polaritons using cathodoluminescence spectroscopy. *Applied Physics Letters*, 88, 2006.
- [18] M.V. Bashevoy, F. Jonsson, A.V. Krasavin, N.I. Zheludev, Y. Chen, and M.I. Stockman. Generation of traveling surface plasmon waves by free-electron impact. *Nano Letters*, 6, 2006.
- [19] N. Yamamoto, K. Araya, and F. J. García de Abajo. Photon emission from silver particles induced by a high-energy electron beam. *Phys. Rev. B*, 64(20):205419, Nov 2001.
- [20] Carrie E. Ross et al. Imaging plasmonic modes in annular nanoresonators using spectrally resolved cathodoluminescence. Submitted Dec. 2006.
- [21] Jean-Claude Weeber, Alain Dereux, Christian Girard, Joachim R. Krenn, and Jean-Pierre Goudonnet. Plasmon polaritons of metallic nanowires for controlling submicron propagation of light. *Phys. Rev. B*, 60(12):9061–9068, Sep 1999.
- [22] D McMullan. An improved scanning electron microscope for opaque specimens. *Proc Inst Electr Engrs*, 100, 1953.
- [23] Jon Orloff. High-resolution focused ion beams. *Rev. Sci. Instrum.*, 64(5), May 1993.
- [24] J. Gupta, J. M. E. Harper, J. L. Mauer, P. G. Blauner, and D. A. Smith. Focused ion beam imaging of grain growth in copper thin films. *Applied Physics Letters*, 61, 1992.
- [25] D.T.J. Hurle and B. Cockayne. *Handbook of Crystal Growth*, volume 2A. Czochralski growth. North-Holland, Amsterdam, 1994.

- [26] Woo Lee, Ran Ji, Ulrich Gösele, and Kornelius Nielsch. Fast fabrication of long-range ordered porous alumina membranes by hard anodization. *Nature Materials*, 2006.
- [27] Joan Penninkhof. *Tunable plasmon resonances in anisotropic metal nanostructures*. PhD thesis, FOM-institute AMOLF, Utrecht University, 2006.
- [28] Kane Yee. Numerical solution of initial boundary value problems involving maxwell's equations in isotropic media. *Antennas and Propagation, IEEE Transactions on*, 14:302–307, May 1966.
- [29] Germany Gesellschaft für Computer-Simulationstechnik (CST), Darmstadt. MAXwell's equations by Finite Integration Algorithm (MaFIA), 2000.
- [30] L. A. Sweatlock, S. A. Maier, H. A. Atwater, J. J. Penninkhof, and A. Polman. Highly confined electromagnetic fields in arrays of strongly coupled Ag nanoparticles. *Physical Review B (Condensed Matter and Materials Physics)*, 71(23):235408, 2005.

Acknowledgements

Many people were involved with the completion of this work, for which I am very grateful. First I would like to mention my direct supervisors, Albert Polman and René de Waele, who managed to push me much farther than I would have come on my own, thanks to your enthusiasm and a lot of help. Also I really appreciate your flexibility.

The Photonic Materials group was a very good place to be. Thank you Sébastien Bidault, Rob van Loon, Femius Koenderink, Martin Kuttge, Hans Mertens, Joan Penninkhof, and Ewold Verhagen for a nice atmosphere and time for discussions. I am looking forward to working with all of you in the future.

This is also very true for Hans Zeijlemaker and Chris Rétif. During the fabrication and experiments you were a fantastic help, and fun to work with.

At Caltech in Pasadena, California, I would like to thank Harry Atwater for allowing me a stay in his group, which was a very special experience. It was an honor and pleasure to work with Henri Lezec at the Focused Ion Beam, thanks Henri for your patience and a very nice introduction to the FIB. I would like to thank Luke Sweatlock and Carrie Ross for helping me setting up the simulations and understanding the results. I would like to thank everyone else in the Atwater group for making my stay so enjoyable by helping in the lab and having fun outside.

I am grateful to prof. Goesele who was willing to cooperate and send us a sample, prepared by Woo Lee at the Max-Planck Institut für Mikrostrukturphysik in Halle, Germany.

Finally I would like to thank my parents. Thank you very much for your support all those years. And of course thank you my dear José. After finishing this thesis I guess it's my turn to cook!